

# On the validity of the Arrhenius picture in two-dimensional submonolayer growth

Joseba Alberdi-Rodriguez<sup>a,b,\*</sup>, Shree Ram Acharya<sup>d</sup>, Talat S. Rahman<sup>a,d</sup>, Andres Arnau<sup>b,c</sup>, Miguel Angel Gosálvez<sup>a,b,c</sup>

<sup>a</sup>Donostia International Physics Center (DIPC), Manuel Lardizabal 4, 20018 Donostia-San Sebastián, Spain

<sup>b</sup>Departamento de Física de Materiales, University of the Basque Country UPV/EHU, Manuel Lardizabal 3, 20018 Donostia-San Sebastián, Spain

<sup>c</sup>Centro de Física de Materiales CFM-Materials Physics Center MPC, centro mixto CSIC UPV/EHU, 20018 Donostia-San Sebastián, Spain

<sup>d</sup>Department of Physics, University of Central Florida, Orlando, FL 32816, USA

---

## Abstract

For surface-mediated processes, such as on-surface synthesis, epitaxial growth and heterogeneous catalysis, a constant slope in the Arrhenius diagram of the corresponding rate of interest against inverse temperature,  $\log R$  vs  $1/k_B T$ , is traditionally interpreted as the existence of a bottleneck elementary reaction (or rate-determining step), whereby the constant slope (or apparent activation energy,  $E_{app}^R$ ) reflects the value of the energy barrier for that reaction. Here, we show that a constant value of  $E_{app}^R$  can be obtained even if control shifts from one elementary reaction to another. In fact, we show that  $E_{app}^R$  is a weighted average and the leading elementary reaction will change with temperature while the actual energy contribution for every elementary reaction will contain, in addition to the traditional energy barrier, a configurational term directly related to the number of local configurations where that reaction can be performed. For this purpose, we consider kinetic Monte Carlo simulations of two-dimensional submonolayer growth at constant deposition flux, where the rate of interest is the tracer diffusivity. In particular, we focus on the study of the morphology, island density and diffusivity by including a large variety of single-atom, multi-atom and complete-island diffusion events for two specific metallic heteroepitaxial systems, namely, Cu on Ni(111) and Ni on Cu(111), as a function of coverage and temperature.

**Keywords:** apparent activation energy, epitaxial growth, surface morphology, island diffusion, kinetic Monte Carlo

---

## 1. Introduction

Two dimensional (2D) materials have attracted interest due to their superior properties and promising applications [1, 2, 3, 4, 5, 6, 7]. However, their future success depends on the ability to achieve production in large amounts and with high-quality, which directly relies on a better understanding of their synthesis by a variety of surface-mediated processes [1]. As an example of the many techniques available, chemical vapour deposition (CVD) can be used to grow a metal on top of the same metal (homoepitaxy) or on a different metal (heteroepitaxy), which is also valid for the synthesis of novel materials, such as graphene [8, 9, 10, 11, 12, 13, 14, 15]. Traditionally, low energy electron diffraction (LEED) [16, 17, 18], field ion microscopy (FIM) [19, 20], scanning tunnelling microscopy (STM) [21] and related microscopies have enabled the observation of single molecules and atoms on the surface, thus providing specific insights regarding the growth process [22, 23, 24, 25, 26].

In general, surface-mediated growth uses a constant flux for each vapour species, which is either adsorbed or

thermally decomposed at the surface. The resulting adparticles diffuse randomly, eventually forming small clusters at random locations (nucleation), which gradually evolve into larger islands through the attachment of other diffusing adparticles (growth) until the islands eventually merge to form a single 2D layer (coalescence). The quality of the 2D material is affected markedly by the density and structure of the formed grain boundaries, directly depending on the actual size and shape of the islands (dendritic, compact, polygonal, ...), which ultimately depends on the relative occurrence of the adsorption and diffusion events. In this context, the natural quantity describing the behaviour of the system is the tracer diffusivity [27].

Due to the general character of the previous surface-mediated growth mechanism, here we study submonolayer heteroepitaxial growth of metals, in order to understand some of the global features, especially the dominant contributions to the apparent activation energy of the diffusivity. In particular, we consider the growth of two heteroepitaxial systems, namely, Cu on Ni(111) and Ni on Cu(111), where the compact and stable (111) surfaces provide a small lattice mismatch with respect to the growing 2D islands ( $\sim 2.5\%$ ), thus facilitating surface diffusion and enabling the achievement of concerted events, i.e. the diffusion of more than one adatom at once. Although

---

\*Corresponding author: joseba.alberdi@ehu.eus

there are theoretical studies on (i) the diffusivity of a single monomer of Cu (Ni) on Ni (Cu) [28, 29] and (ii) a more complete growth picture of Cu/Ni(111) [30, 31] and Ni/Cu(111) [32, 33, 34], in this study we consider a large variety of single-atom, multi-atom and complete-island diffusion events, with the aim of obtaining a general picture on the relative importance of concerted diffusion in two-dimensional material growth, applied to metals.

The growth process is simulated by using the kinetic Monte Carlo (KMC) method [35, 36]. As opposed to molecular dynamics (MD), the KMC method avoids following the motion of every possible atom contained in the system, simply recognising that the important events—which modify the configuration of the system and not just a few bond lengths—correspond to the elementary reactions, each occurring after a certain wait time. In this manner, every distinct elementary reaction (or rare event) is assigned a different rate and time is discretised, with the resulting time increment being much larger than in MD, thus enabling much longer simulation times. Based on a many body semi empirical embedded atom model for the description of the interaction between the atoms [37], the diffusion energy barriers,  $E_\alpha^k$ , required to compute the rate of each distinct diffusion event, are obtained by using the drag method [38, 39]. The simulations allow switching on and off the concerted events as desired, thus enabling the study of their relative importance against other events, including their contribution to the apparent activation energy, as well as their effect on the morphology of the generated islands.

In this respect, the actual shapes of the islands typically look different from one simulation to another, due to the stochastic nature of the KMC method. However, the simulations performed using the same rates (= rate constants) display common features and simple visual inspection will conclude that the islands are equivalent in some manner. In the present study, this is demonstrated quantitatively by performing a power spectral density (PSD) analysis [40, 41, 42, 43]. Here, an image of the surface is associated with a 2D map, where each location represents a harmonic frequency and the displayed value represents the squared sum of the real and imaginary amplitudes for that harmonic component (i.e., the power for that frequency). Low frequencies are correlated to large structures, such as the overall shape of the islands, while large frequencies are related to small features, such as the structure of the perimeter. In this manner, the PSD analysis enables comparing different/similar surfaces with stochastic variations. In fact, two PSD maps can be considered equivalent when their point-to-point difference produces noise (= stochastic fluctuations) around the 0 value all over the resulting difference map. On the contrary, when two PSDs differ structurally, their difference map displays distinctive patterns, clearly deviating from random fluctuations around the 0 value. This enables determining the effect on the morphology of the generated islands due to switching on or off certain diffusion events.

In order to describe the dominant contributions to the apparent activation energy of the tracer diffusivity, section 2.1 presents the direct relation that exists between the diffusivity and the total diffusion rate (= total hop rate). The total diffusion rate, in turn, depends directly on the multiplicities of the different diffusion events (i.e., the multiplicity is the actual number of locations where each distinct diffusion event can be performed in a given snapshot of the surface). This is followed by a description of all the different diffusion events considered in the study, including single-atom, multi-atom and complete-island diffusion events as well as their energy barriers in sections 2.2-2.3. For clarity, section 2.4 provides a detailed description of the total diffusion rate, total adsorption rate and total rate as well as their time and ensemble averages in terms of the corresponding multiplicities, and section 2.5 shows, as a result, that the apparent activation energy of any of the total rates depends on the multiplicities and, thus, the apparent activation energy of the diffusivity as well. Finally, section 2.6 culminates the presentation of the theoretical and computational aspects of the study by describing the most salient features of the implemented KMC method. In addition, sections 3.1-3.4 present the results of the study, comparing the temperature dependence of the island density, morphology, total rates and their apparent activation energy for the two chosen systems, namely, Cu on Ni(111) and Ni on Cu(111). Finally, section 4 summarises the conclusions of the study.

## 2. Computational details and theoretical aspects

### 2.1. Tracer diffusivity in surface-mediated growth

The natural quantity describing submonolayer growth under a constant flux of adparticles is the tracer diffusivity [27]:

$$D_T = \frac{1}{2\delta\langle\hat{n}_a\rangle} \frac{\langle\hat{\mathcal{R}}^2\rangle}{t}, \quad (1)$$

where the hat symbol ( $\hat{\phantom{x}}$ ) denotes the value of a time-dependent variable at time  $t$ ,  $\delta$  is the dimensionality (= 2 for diffusion on a surface),  $\hat{n}_a$  is the number of adsorbed particles,  $\hat{\mathcal{R}}^2 = \sum_{i=1}^{\hat{n}_a} |\hat{\mathbf{x}}_i - \mathbf{x}_i^*|^2$  is the total squared distance travelled by the adparticles, with  $\mathbf{x}_i^*$  denoting the position of adparticle  $i$  when it was adsorbed, and  $\langle\hat{X}\rangle$  is the ensemble average of  $\hat{X}$  over  $K$  samples in the limit of large  $K$ . In particular, the diffusivity can be re-written as [27]:

$$D_T = \frac{l^2}{2\delta\hat{\theta}} f_T R_d, \quad (2)$$

$$R_d = \sum_{\alpha \in \{d\}} M_\alpha k_\alpha, \quad (3)$$

where  $l$  is the hop distance between adjacent sites,  $\theta = \langle\hat{\theta}\rangle$  is the ensemble average of the coverage,  $\hat{\theta} = \hat{n}_a/L_x L_y$ , with  $L_x L_y$  being the total number of adsorption sites,  $R_d = \langle\hat{R}_d\rangle$  is the time and ensemble average of the total

diffusion rate per site,  $\hat{R}_d$ , where  $\overline{\hat{X}} = \frac{\int \hat{X} dt}{\int dt} = \frac{\sum_k \hat{X}_k \Delta t_k}{\sum_k \Delta t_k}$  is the time average of  $\hat{X}$ , and  $f_T$  is the correlation factor, which accounts for memory effects between consecutive hops at finite coverages, *e.g.* hopping from site  $i$  to site  $j$  leaves site  $i$  empty and, thus, at finite coverage the adparticle has a higher chance of returning to  $i$  [27]. Finally, equation 3 is the time and ensemble average of:  $\hat{R}_d = \sum_{\alpha \in \{d\}} \hat{M}_\alpha k_\alpha$ , which defines the total diffusion rate per site. The summation is over the collection of all distinct diffusion events  $\{d\}$ ,  $k_\alpha$  is the rate of diffusion event  $\alpha$  (referred to as the *rate constant* or *specific rate* in chemical kinetics) and  $M_\alpha = \langle \hat{M}_\alpha \rangle$  is the time and ensemble average of the multiplicity,  $\hat{M}_\alpha = \hat{m}_\alpha / L_x L_y$ , with  $\hat{m}_\alpha$  being the number of locations where diffusion event  $\alpha$  can be performed in a given snapshot of the surface. Here,  $k_\alpha$  is determined by using transition state theory (TST):

$$k_\alpha = k_0 e^{-E_\alpha^k / k_B T}, \quad (4)$$

where  $k_B$  is the Boltzmann constant,  $T$  is the temperature,  $E_\alpha^k$  is the energy barrier for the diffusion event and  $k_0$  is the attempt frequency, which depends weakly on temperature and is usually assigned the value of  $10^{13}$  Hz.

Equation 2 means that the apparent activation energy of the diffusivity is essentially given by that of the total diffusion rate. In fact, using equation 3 in equation 2 and denoting the inverse temperature as  $\beta = 1/k_B T$  while considering that the coverage is independent of temperature (due to the constant flux), the apparent activation energy of the diffusivity,  $E_{app}^{D_T} = -\frac{\partial \log D_T}{\partial \beta}$ , is easily determined [27]:

$$E_{app}^{D_T} = E^f + E_{app}^{R_d}, \quad (5)$$

$$E_{app}^{R_d} = \sum_{\alpha \in \{d\}} \omega_\alpha^{R_d} (E_\alpha^k + E_\alpha^M), \quad (6)$$

$$\omega_\alpha^{R_d} = \frac{M_\alpha k_\alpha}{R_d} = \frac{M_\alpha k_\alpha}{\sum_{\alpha' \in \{d\}} M_{\alpha'} k_{\alpha'}}, \quad \alpha \in \{d\}. \quad (7)$$

Here,  $E^f = -\frac{\partial \log f_T}{\partial \beta}$ ,  $E_\alpha^k = -\frac{\partial \log k_\alpha}{\partial \beta}$  and  $E_\alpha^M = -\frac{\partial \log M_\alpha}{\partial \beta}$  are the contributions from the correlation factor ( $f_T$ ), the rate of diffusion event  $\alpha$  ( $k_\alpha$ ) and the corresponding multiplicity ( $M_\alpha$ ), respectively, and the weight  $\omega_\alpha^{R_d}$  is the *probability* of observing diffusion event  $\alpha$  amongst all distinct diffusion events. Indeed, the *event probabilities* of equation 7 are very useful, providing a complete picture of the undergoing competition between the different diffusion events, directly indicating which events dominate and which are essentially irrelevant. Typically, the contribution from the correlation factor is small ( $E^f \approx 0$ ) [27]. Thus, equation 5 shows that the temperature dependence of the diffusivity is essentially given by that of the total diffusion rate:  $E_{app}^{D_T} = E^f + E_{app}^{R_d} \approx E_{app}^{R_d} = \sum_{\alpha \in \{d\}} \omega_\alpha^{R_d} (E_\alpha^k + E_\alpha^M)$ . In this manner, we focus below on the analysis of the total diffusion rate.

## 2.2. Identification of diffusion events

The diffusion of adsorbates on a substrate is an essential part of film growth. In general, a diffusion event may consist in a single-atom hop (single-atom diffusion), a complete-island hop (concerted island diffusion) or a multi-atom hop at the perimeter of a compact island (concerted multi-atom diffusion) [44, 45, 46, 47, 48, 49, 50]. Here, an island is considered as a structure where each atom is connected with at least one nearest neighbour. Based on an extensive study of post-adsorption diffusion kinetics of small islands of Cu/Ni(111) and Ni/Cu(111) as a function of the island size [28, 39], it is concluded that, in addition to single-atom diffusion, the most executed diffusive events correspond to concerted diffusion of complete islands with size up to eight atoms and concerted two-atom diffusion along the step-edge of compact islands. Thus, the current study focuses on including these particular diffusion events.

The crystallographic structure of the fcc(111) surface under consideration in this study is described by a triangular lattice, where every node represents an adsorption site. Any site is assigned a type (the unique combination of a class and a subclass), regardless of being occupied by an atom or not. The site class directly indicates the number of occupied nearest neighbour sites, and the subclass is simply a label that allows distinguishing between the different geometrical arrangements of the occupied neighbour sites. As shown in figure 1, we consider 7 site classes (from 0 to 6) and a maximum of 3 subclasses (from 0 to 2), leading to a total of 13 site types. The subclass is always 0 for classes 0, 1, 5 and 6, while it is arbitrarily and consistently assigned the value 0, 1 or 2 for classes 2, 3 and 4, depending on the geometrical arrangement.












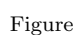
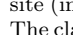
| type  | class | subclass | type  | class | subclass |
|---|-------|----------|---|-------|----------|
|  | 0     | 0        |  | 8     | 4        |
|  | 1     | 0        |  | 9     | 4        |
|  | 2     | 0        |  | 10    | 4        |
|  | 3     | 2        |  | 11    | 5        |
|  | 4     | 2        |  | 12    | 6        |
|  | 5     | 3        |   |       |          |
|  | 6     | 3        |   |       |          |
|  | 7     | 3        |   |       |          |

Figure 1: Site types considered in this study, indicated for the central site (in red). The type is a unique combination of class and subclass. The class directly indicates the number of occupied nearest neighbour sites (in green). The subclass is a label used to distinguish between different geometrical arrangements of the occupied neighbours.

For any particular diffusion event, the destination site is assigned the site type by considering that the atom has already hopped on it. Thus, for a destination site, the class and subclass are determined by considering the origin site as being empty. This is shown in figure 2. For the first column, the destination site will have no occupied neighbours and, thus, the type is 0 (class 0, subclass 0); for the second column, the destination site will have one

occupied neighbour and, therefore, the type is 1 (class 1, subclass 0); and so on. Note that, in practice, there are only 12 origin types (0 to 11), since diffusion is impossible from type 12 (class 6, subtype 0). Furthermore, regarding the destination types, we consider some additional cases in order to take into account detachment events. Here, detachment means that the destination site has no neighbours in common with the origin site. This leads to a total of 16 destination types, as shown in figure A1 of the appendix. Consequently, we work with a transition table of  $12 \times 16$  entries, where the rows correspond to the origin site types and the columns to the destination site types.

In order to assign a type to a diffusion event, we use the origin and destination types of the involved sites. Some representative single-atom diffusion events are shown in figure 2, where the atom at the origin site (in red) is moved one site to the right in each of the 15 examples. In this manner, monomer diffusion is described by a hop from type 0 to type 0 ( $D[0,0] \rightarrow [0,0]$ ), while edge diffusion is described by a hop from type 2 to type 3 ( $D[2,0] \rightarrow [2,0]$ ). Note that some transitions are physically impossible and, thus, not displayed. Similarly, we do not display the symmetry equivalent transitions for the other five hop directions (there are 6 possible directions in a triangular lattice), since all directions are treated identically.

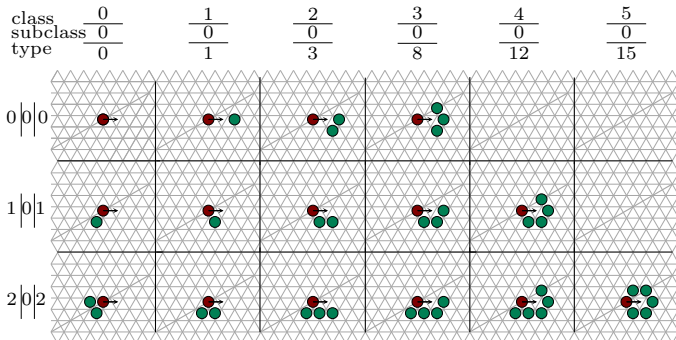


Figure 2: An extract of the total transition table for single-atom diffusion on a triangular lattice, showing a few representative origin site types (rows) and destination site types (columns). In all cases the red particle moves one lattice site to the right. The complete table appears in figure A1 of the appendix.

In addition to single atom hops, we include concerted island diffusion up to 8 atoms, where all the atoms belonging to the island move together in one of the six directions, independently of the island shape. For the calculation of the corresponding energy barrier (see section 2.3) the most compact shapes are used, as shown in figure 3a. For instance, this means that all different trimer shapes have the same rate to move in any direction. Finally, we also include concerted two-atom diffusion along the perimeter of compact islands according to the four different event types shown in figure 3b. Overall, we consider 118 different diffusion event types: 107 single-atom diffusions (figure A1 of the appendix), 7 complete-island moves (figure 3a) and 4 multi-atom hops (figure 3b).

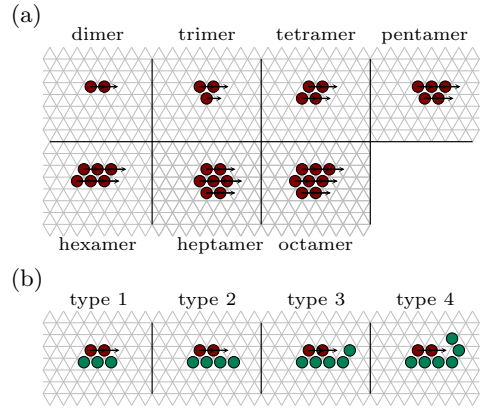


Figure 3: (a) Compact islands containing up to 8 atoms, used for the calculation of the diffusion energy barrier for concerted island diffusion. (b) Concerted diffusion events for two-atoms (in red) at the perimeter of an island (in green), classified according to the destination site type for the rightmost diffusing atom.

### 2.3. Calculation of energy barriers and rates

For each identified diffusion event, the activation energy barrier ( $E_{\alpha}^k$ ) is calculated by using the drag method while describing the interaction between the atoms with a many-body semi-empirical embedded atom model (EAM) [37]. The EAM + drag combination produces qualitative and semi-quantitative results with minor errors for metallic systems when compared with ab initio energetics, including island diffusion barriers on fcc(111) [28, 38]. For this study, the substrate consists on five fcc(111) layers with  $16 \times 16 = 256$  atoms per layer, where the two bottom layers are kept frozen (to mimic the bulk) while the three top layers are allowed to relax. For each diffusion event, the required adatoms are placed on the surface on the desired initial configuration and the system is relaxed (standard MD cooling with velocity updates using the leap-frog algorithm) until the energy change between successive updates is less than  $10^{-4}$  eV, taking the corresponding minimised energy as reference for the calculation of  $E_{\alpha}^k$ .

In order to determine the energy barrier for a single-atom diffusion event, the chosen adatom is gradually dragged in steps of  $0.05 \text{ \AA}$  along the reaction coordinate, whose direction is re-defined at every step as the vector from the relaxed location of the adatom to the aimed location in the final configuration. At every step, relaxation is allowed for the dragged adatom along the plane perpendicular to the current direction of the reaction coordinate while keeping fixed all other adatoms, the two bottom layers and the reaction coordinate, until the energy difference is less than  $10^{-3}$  eV (1 meV) or the relaxed adatom is  $0.05 \text{ \AA}$  from the aimed location. The maximum energy point in the energy profile of the minimum energy path represents the saddle point and its energy difference from the reference energy gives  $E_{\alpha}^k$  for the diffusion event. For multi-atom and concerted diffusion events, the same procedure is applied to the adatoms under consideration. See Ref. [39] for further details.



The computed energy barriers are displayed in tables A1 and A2 of the appendix. The barriers for monomer diffusion are within the expected range, compared with the literature [22]. Our diffusion barrier of 52 meV for Cu on Ni(111) is virtually the same as the previously reported value of 50 meV [51]. For diffusion of Ni on Cu(111), we obtain 31 meV, which is about 2/3 of the value (45 meV) reported in Ref. [51]. Once the energy barrier  $E_\alpha^k$  has been obtained for diffusion event  $\alpha$ , the corresponding diffusion rate ( $k_\alpha$ ) is computed by using equation 4.

#### 2.4. Total rates and the probability to observe an event

In order to model the adsorption and diffusion of adatoms of Ni on Cu(111) and Cu on Ni(111), we consider a two-dimensional lattice of adsorption sites under a typical constant deposition flux [27, 52, 53, 54, 55]. For each of the two systems, the substrate is treated as a two-dimensional triangular lattice, where atoms from the surrounding environment are deposited randomly (on the empty sites) while previously adsorbed adatoms are able to diffuse according to the particular diffusion events considered in section 2.3 for single atoms, multiple atoms and complete islands. Desorption events are neglected, due to their extremely low rate in these systems. A constant deposition flux,  $F$ , is considered at any temperature and, thus, a temperature-independent adsorption rate per site is used,  $k_a = F$ , independently of the occupation state of the neighborhood of the empty site where adsorption may occur. For diffusion, the temperature-dependent diffusion rate for event type  $\alpha$ ,  $k_\alpha$ , is given by equation 4. Below, instantaneous values of time-dependent variables are indicated by using the hat symbol ( $\hat{\cdot}$ ). The theoretical presentation provided below follows closely that given in Ref. [56].

At any given time  $t$ , the total diffusion rate is:

$$\hat{r}_d = \sum_{\alpha \in \{d\}} \hat{m}_\alpha k_\alpha, \quad (8)$$

where  $\hat{m}_\alpha$  is the multiplicity for diffusion event  $\alpha$ , i.e. the number of locations where that particular diffusion event can be performed on the current configuration of the surface,  $k_\alpha$  is the corresponding diffusion rate, and  $\{d\}$  is the complete collection of distinct diffusion events. Similarly, the total adsorption rate is:

$$\hat{r}_a = \sum_{\alpha \in \{a\}} \hat{m}_\alpha k_\alpha, \quad (9)$$

$$= \hat{m}_a k_a, \quad (10)$$

$$= (1 - \hat{\theta}) L_x L_y k_a = L_x L_y e^{-k_a t} k_a, \quad (11)$$

where  $\{a\}$  is the collection of distinct adsorption events, and  $\hat{m}_\alpha$  ( $k_\alpha$ ) is the corresponding multiplicity (adsorption rate). Since we consider only one adsorption event type, the summation in equation 9 is reduced to a single term, as indicated in equation 10. Here,  $k_a = F$  and  $\hat{m}_a$  is the corresponding multiplicity, i.e. the total number of empty sites. Note that  $\hat{m}_a = (1 - \hat{\theta}) L_x L_y$  in equation 11, where

$\hat{\theta} = \hat{n}_a / L_x L_y$  designates the coverage, with  $\hat{n}_a$  being the total number of adsorbed atoms up to the current time (i.e. the total number of adsorption events) and  $L_x L_y$  the total number of adsorption sites (before adsorption of any atom). Due to the constant deposition flux, the coverage increases with time according to the equation:  $\frac{d\hat{\theta}}{dt} = k_a(1 - \hat{\theta})$ , which is directly integrated to give:  $\hat{\theta} = 1 - e^{-k_a t}$ . Thus,  $\hat{m}_a = L_x L_y e^{-k_a t}$  independently of the temperature.

Finally, since both diffusion and adsorption events may occur, we consider the total rate:

$$\hat{r} = \sum_{\alpha \in \{e\}} \hat{m}_\alpha k_\alpha, \quad (12)$$

$$= \sum_{\alpha \in \{d\}} \hat{m}_\alpha k_\alpha + \sum_{\alpha \in \{a\}} \hat{m}_\alpha k_\alpha, \quad (13)$$

$$= \sum_{\alpha \in \{d\}} \hat{m}_\alpha k_\alpha + \hat{m}_a k_a, \quad (14)$$

$$= \hat{r}_d + \hat{r}_a, \quad (15)$$

where  $\{e\}$  is the collection of all distinct event types (diffusion and adsorption). The total number of performed events is:  $\hat{n} = \hat{n}_d + \hat{n}_a$ , where  $\hat{n}_d$  is the total number of performed hops and  $\hat{n}_a$  is the total number of executed adsorptions (as defined above).

Dividing by the total number of sites,  $L_x L_y$ , we also define the *total diffusion rate per site*,  $\hat{R}_d = \hat{r}_d / L_x L_y$ , the *total adsorption rate per site*,  $\hat{R}_a = \hat{r}_a / L_x L_y$ , the *total rate per site*,  $\hat{R} = \hat{r} / L_x L_y$ , and the *multiplicity per site*,  $\hat{M}_\alpha = \hat{m}_\alpha / L_x L_y$ . For simplicity, both  $\hat{m}_\alpha$  and  $\hat{M}_\alpha$  are referred to as the *multiplicity*, although  $\hat{M}_\alpha$  should be understood as a multiplicity density or relative abundance or concentration. Similarly,  $\hat{R}_d$ ,  $\hat{R}_a$  and  $\hat{R}$  may be referred to as the *total rates*, thus obviating their per-site character. The total diffusion rates,  $\hat{r}_d$  and  $\hat{R}_d$ , are important, since the tracer diffusivity,  $D_T$ , is proportional to their average, as shown in equation 2. Similarly,  $\hat{r}$  and  $\hat{R}$  are also important, since the inverse of  $\hat{r}$  provides a natural measure of the time increment:  $\Delta t = -\log(u) / \hat{r}$ , where  $u \in (0, 1]$  is a uniform random number. By definition,  $\hat{r}$  is equal to the number of performed events per unit time,  $\hat{r} = \frac{d\hat{n}}{dt}$ , and thus,  $\hat{r} = \frac{1}{\Delta t}$ , since exactly one event occurs in every time step. With a mean value of 1, the positive factor  $-\log(u)$  enforces the correct Poisson distribution for the time steps.

Making the observation that  $\hat{r}_d$  is equal to the number of performed diffusion events per unit time,  $\hat{r}_d = \frac{d\hat{n}_d}{dt}$  (similar to  $\hat{r} = \frac{d\hat{n}}{dt}$ ), the time average of  $\hat{r}_d$  for any desired period is written exactly as the total number of performed diffusion events,  $\hat{n}_d$ , divided by the elapsed time,  $t$  (and similarly for  $\hat{r}_a$  and  $\hat{r}$ ):

$$\overline{\hat{r}_d} = \frac{\int \hat{r}_d dt}{\int dt} = \frac{\int \frac{d\hat{n}_d}{dt} dt}{t} = \frac{\int d\hat{n}_d}{t} = \frac{\hat{n}_d}{t}, \quad (16)$$

$$\overline{\hat{r}_a} = \frac{\hat{n}_a}{t}, \quad (17)$$

$$\overline{\hat{r}} = \frac{\hat{n}}{t}. \quad (18)$$

Carrying out the ensemble average in Eqs. 16-18 and dividing by  $L_x L_y$  gives:

$$R_d = \frac{N_d}{\tau}, \quad (19)$$

$$R_a = \frac{N_a}{\tau}, \quad (20)$$

$$R = \frac{N}{\tau}, \quad (21)$$

where  $R_d = \langle \overline{\hat{R}_d} \rangle$ ,  $R_a = \langle \overline{\hat{R}_a} \rangle$  and  $R = \langle \overline{\hat{R}} \rangle$  are the *average total rates per site* (for diffusion, adsorption and all events, respectively), while  $N_d = \langle \hat{n}_d \rangle / L_x L_y$ ,  $N_a = \langle \hat{n}_a \rangle / L_x L_y$ , and  $N = \langle \hat{n} \rangle / L_x L_y$  specify the ensemble averages of the numbers of performed events per site (for diffusion, adsorption and all events, respectively), and  $\tau = \langle t \rangle$  is the ensemble average of the elapsed time. On the other hand, performing the time and ensemble averages on equations 10, 8 and 12 and dividing by the total number of adsorption sites gives:

$$R_d = \sum_{\alpha \in \{d\}} M_\alpha k_\alpha, \quad (22)$$

$$R_a = M_a k_a = (1 - \theta)F, \quad (23)$$

$$R = R_d + R_a = \sum_{\alpha \in \{e\}} M_\alpha k_\alpha, \quad (24)$$

where  $M_\alpha = \langle \overline{\hat{m}_\alpha} \rangle / L_x L_y$  and  $M_a = \langle \overline{\hat{m}_a} \rangle / L_x L_y = 1 - \theta$  are the corresponding time and ensemble averages of the multiplicities per site. Here,  $\theta = \langle \hat{\theta} \rangle$  is the ensemble average of the coverage. Equations 19-21 and 22-24 are very important for this study, since they provide two alternative expressions to determine the same quantities ( $R_d$ ,  $R_a$  and  $R$ ). In addition to ensuring the correct determination of each quantity, the equations provide a way to describe the particular contributions that make up any specific value of their apparent activation energy.

Finally, we note that, in addition to the relation to the time increment, the average total rate per site,  $R$ , is very important, since it is used in the definition of the *probability* of observing event  $\alpha$  amongst all distinct events (diffusion and adsorption):

$$\omega_\alpha^R = \frac{M_\alpha k_\alpha}{R} = \frac{M_\alpha k_\alpha}{\sum_{\alpha' \in \{e\}} M_{\alpha'} k_{\alpha'}}, \quad \alpha \in \{e\}. \quad (25)$$

Note the difference with respect to  $\omega_\alpha^{R_d}$  in equation 7. Although both quantities are probabilities, their meaning is with respect to the collection of events considered in the

denominator, thus justifying the superindex  $R$  or  $R_d$ , respectively. The *event probabilities* of equation 25 directly indicate which events dominate the overall process, considering both adsorption and diffusion events. The *event probabilities* of equation 7 indicate which diffusion events dominate with respect to all distinct diffusion events. Due to the link of  $R$  to the overall event probabilities and of  $R_d$  to the tracer diffusivity, we focus on the analysis of the temperature dependence of both quantities.

### 2.5. Apparent activation energy

For an Arrhenius plot of the average total rate per site [where  $\log(R)$  is drawn against inverse temperature,  $\beta = 1/k_B T$ ], the apparent activation energy is defined as:

$$E_{app}^R = -\frac{\partial \log R}{\partial \beta}, \quad (26)$$

$$= -\frac{1}{R} \frac{\partial R}{\partial \beta}, \quad (27)$$

$$= -\frac{1}{\sum_{\alpha \in \{e\}} M_\alpha k_\alpha} \frac{\partial (\sum_{\alpha \in \{e\}} M_\alpha k_\alpha)}{\partial \beta}, \quad (28)$$

where equation 24 has been used to write equation 28. Since the multiplicities,  $\hat{m}_\alpha$ , depend on the actual values of the event rates,  $k_\alpha$ , the average multiplicities per site,  $M_\alpha$ , are functions of temperature. Using  $k_\alpha = k_\alpha^0 e^{-E_\alpha^k \beta}$  and  $E_\alpha^M = -\frac{\partial \log M_\alpha}{\partial \beta}$ , and applying the chain rule to  $\sum_{\alpha \in \{e\}} M_\alpha k_\alpha$  easily leads to:

$$E_{app}^R = \sum_{\alpha \in \{e\}} \epsilon_\alpha^R, \quad \text{with } \epsilon_\alpha^R = \omega_\alpha^R (E_\alpha^k + E_\alpha^M), \quad (29)$$

where the weight  $\omega_\alpha^R$  is the probability to observe event  $\alpha$ , as given in equation 25. Note that, in general, the additional term  $E_\alpha^{k^0} = -\frac{\partial \log(k_\alpha^0)}{\partial \beta}$  should be added to  $E_\alpha^k + E_\alpha^M$  in equation 29. However,  $E_\alpha^{k^0}$  is zero in this study, since the prefactors  $k_\alpha^0$  are temperature-independent.

According to equation 29, the contribution of event type  $\alpha$  to the apparent activation energy is  $\epsilon_\alpha^R = \omega_\alpha^R (E_\alpha^k + E_\alpha^M)$ . Simply speaking,  $\omega_\alpha^R$  provides the relative importance of event type  $\alpha$  as compared to all other events. Inside the bracket, the microscopic activation energy for the event type,  $E_\alpha^k$ , is modified by a configurational contribution,  $E_\alpha^M$ , which describes how the multiplicity of that event type changes with temperature. Note that  $E_\alpha^M$  is unbounded and can be positive, negative or zero, depending on the actual increase, decrease or constancy of  $M_\alpha$  locally with respect to temperature. Thus, when the overall process is dominated by a single event type or *rate determining step*, say  $\lambda$ , then  $\omega_\lambda^R \approx 1$  and  $\omega_\alpha^R \approx 0$  for all other event types, and we have:  $E_{app}^R = E_\lambda^k + E_\lambda^M$ . In this manner, the apparent activation energy,  $E_{app}^R$ , differs from the activation barrier of the rate determining step,  $E_\lambda^k$ , due to the change in the number of locations where that particular event can be performed on the surface as a function of temperature,  $E_\lambda^M$ .

The apparent activation energy  $E_{app}^{R_d}$  of the total diffusion rate,  $R_d$ , is obtained similarly and the result is given in equation 6. Thus, the apparent activation energies for  $R$  and  $R_d$  have the same functional dependence, only differing in the actual collection of considered events (both diffusion and adsorption events for  $R$ , and only the diffusion events for  $R_d$ ) and, correspondingly, the value of the weight, i.e. the probability with respect to the other considered events.

### 2.6. Kinetic Monte Carlo

For the actual simulations, we use the standard, rejection-free, time-dependent implementation of the kinetic Monte Carlo (KMC) method with periodic boundary conditions [27, 35, 38, 28, 43]. A flowchart of the KMC procedure is presented in figure 4. Regarding the central rhombus in figure 4, a threefold termination criterion is used, based on surpassing any of the maximum values specified by the user for (i) the coverage  $\hat{\theta}$ , (ii) the simulated time  $t$ , and (iii) the total number of simulated events  $\hat{n} = \hat{n}_d + \hat{n}_a$ . In order to initiate the simulation (and keep it going) the fundamental ingredients are the combination of a specific geometry (figure 4I, here a triangular lattice), a complete list of possible events (figure 4II.) and their rates (figure 4III.). Although nothing prevents starting from an arbitrary coverage, in this study the initial configuration is always an empty surface (no adatoms).

Initially, the stop criteria are not met and the main loop starts by updating the simulated time (figure 4a.). This is done by adding the time increment  $\Delta t = -\log(u)/\hat{r}$  to the current value of  $t$ , as indicated in section 2.4. Continuing with the algorithm, a random number is used to select the next event that will be executed (figure 4b.). This is done by randomly choosing one rate among all the current rates, i.e. among all the diffusion and adsorption events that are currently possible. The next step in the algorithm is to execute the selected event (figure 4c.). From a computational perspective, adsorption implies adding an atom to an empty site while, in general, diffusion requires removing several atoms from the occupied initial sites and adding them to the empty final sites. As a result, the adsorption and diffusion rates need to be updated for the involved sites as well as their neighbours (figure 4d.), adding and deleting available events too. The main loop finishes here and it is repeated until a stop criterion is met.

For this study we have used the software known as “Morphokinetics”, written in object-oriented Java language and developed at the Donostia International Physics Center. Based on the KMC method, Morphokinetics enables simulating various surface-mediated processes, including anisotropic etching (removal of material from the substrate), heterogeneous catalysis (reactions on the substrate) and 2D monolayer growth (deposition of material on the substrate). The source code is freely available at the GitHub repository <sup>1</sup>, with a free license GNU General Public Li-

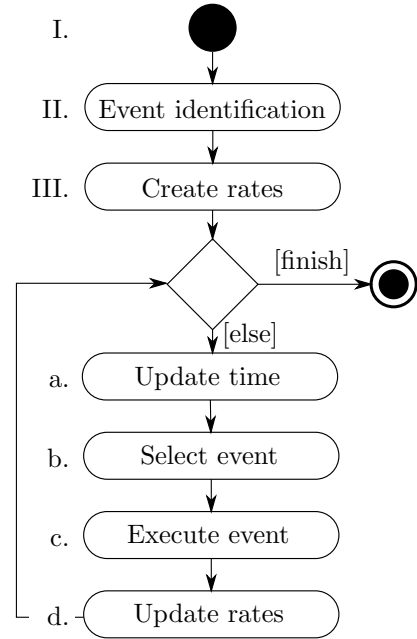


Figure 4: Unified modelling language (UML) activity diagram of a generic KMC algorithm.

cence version 3 or any later version, which means that users have freedom to run, study, redistribute and improve the program.

In the simulations, the adsorption flux is fixed to  $1.5 \times 10^4$  ML/s and the temperature is varied from 23 to 1000 K for both systems under study. We use just one value of the flux, since the behaviour of the system is the same for other values by simply shifting the temperature range [27]. The simulated surfaces contain  $283 \times 283$  Cartesian units, corresponding to  $L_x \times L_y = 283 \times 326 = 92258$  adsorption sites in the triangular lattice, and periodic boundary conditions are applied. The simulations are evolved until 100 % coverage ( $\theta = 1$  ML), repeating them  $K = 10$  times in order to obtain ensemble averages for all quantities of interest. Strictly two-dimensional growth is simulated (no three-dimensional features are attempted). Snapshots of the surface configuration are obtained every 5 % of coverage, which are used as input for the morphology analysis (see the end of section 1).

## 3. Results

### 3.1. Island density

We first consider the island density,  $\langle n_{isl} \rangle$ , defined for any given coverage as the ensemble average of the total number of islands divided by the total number of adsorption sites  $L_x L_y$ . Figure 5a shows that  $\langle n_{isl} \rangle$  is higher for Cu/Ni(111) than for Ni/Cu(111) in all the temperature range, except for the highest temperatures. The plot corresponds to 10 % coverage ( $\theta = 0.10$ ), which is low enough to avoid potential coalescence of neighbour islands, while it is high enough to ensure the formation of stable islands.

<sup>1</sup><https://github.com/dipc-cc/Morphokinetics.git>

For both systems, the lower the temperature the larger the island density and, overall, the temperature dependence is similar. Nevertheless, for the same coverage and temperature, the particular value of the density is different.

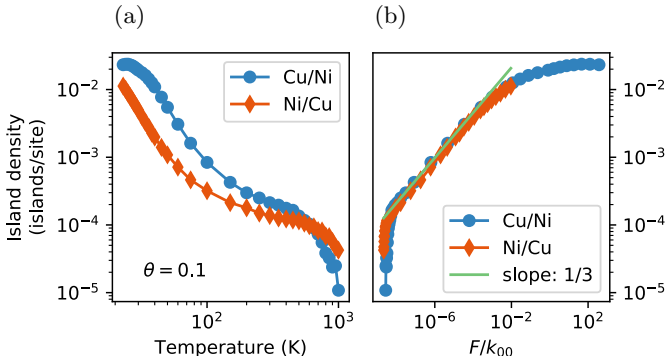


Figure 5: Average island density at 10 % coverage for Cu/Ni(111) and Ni/Cu(111) from 23 K to 1000 K with concerted island and multi-atom diffusion events activated.

This behaviour agrees well with traditional 2D nucleation theory [57, 22]:

$$n_{\text{isl}} \propto \left( \frac{F}{D} \right)^{\frac{i}{i+2}}, \quad (30)$$

where  $F$  is the adsorption flux,  $D = \frac{1}{2\delta} \langle \mathcal{R}^2 \rangle_t$  is the diffusivity for a single monomer ( $D = \frac{3}{4} k_m l^2$  for the triangular lattice, with  $k_m$  the monomer diffusion rate and  $l = 1$  the hop distance) and  $i$  is the critical island size (islands with size  $> i$  are stable). In our case, the deposition flux  $F$  takes the same value and the critical island size  $i$  behaves practically the same in both systems (see next paragraph). However,  $D \propto k_m$  varies with the adatom type (Ni or Cu) and temperature. In fact, the monomer diffusion energy barrier is 52 meV for Cu/Ni(111) and 31 meV for Ni/Cu(111), which implies higher  $D$  for the Ni/Cu(111) system and, thus, lower island density. Therefore, the observed behaviour with temperature agrees with expectations, except at the highest temperatures, where diffusion is not controlled anymore by the monomers and the critical island size deviates from one system to the other.

In fact, the plot of  $\log(n_{\text{isl}})$  vs  $\log(F/k_m)$  in figure 5b shows that the two systems follow equation 30, with  $i = 1$  and  $x = \frac{i}{1+i} = \frac{1}{3}$  at medium temperatures (= medium  $F/k_m$ ). This means that dimers are the smallest stable nuclei in this range. At low temperatures (high  $F/k_m$ ),  $n_{\text{isl},\text{Ni}}$  displays a tendency towards saturation, indicating that  $i \approx 0$  for extremely low temperatures, i.e. monomers already form stable nuclei. This is due, literally, to the absence of diffusion and the dominant role of adsorption, as will be shown in section 3.3. Note that  $n_{\text{isl},\text{Cu}}$  shows the same tendency at low temperatures. In turn, at high temperatures (low  $F/k_m$ ), the slopes of  $n_{\text{isl},\text{Ni}}$  and  $n_{\text{isl},\text{Cu}}$  increase dramatically while slightly deviating from each other, indicating, as expected, that significantly more than two adatoms are required to stabilise a cluster and the

actual diffusion events contributing to the stabilisation of the nuclei differ slightly from one system to the other.

### 3.2. Morphology

Not only the island density differs from one system to the other, their morphology deviates as well. This is shown in figures 6b and 6e for a collection of representative temperatures at  $\theta = 0.10$ . At the lower temperatures the islands are more dendritic in both systems, reflecting low diffusivity along the island perimeters after monomer attachment. At the higher temperatures, however, the islands tend to be compact/hexagonal, reflecting high diffusivity at the perimeters. In this case, the adatoms move quickly along the perimeters and are able to find the lowest energy sites (or thermodynamically stable positions).

The morphology of the islands reflects differences in the growth process. Simple visual inspection indicates that the island shapes are different, specially at 350 K, where Cu forms compact islands while Ni condensates into dendritic shapes. At the other temperatures, however, the distinction is less obvious and a quantitative PSD analysis is required to show the actual variations. By using the images from  $K = 10$  equivalent simulations with different random numbers, the corresponding PSD maps are shown in figure 6a for Cu/Ni(111) and figure 6d for Ni/Cu(111). In addition, point-by-point PSD difference maps are shown in figure 6c.

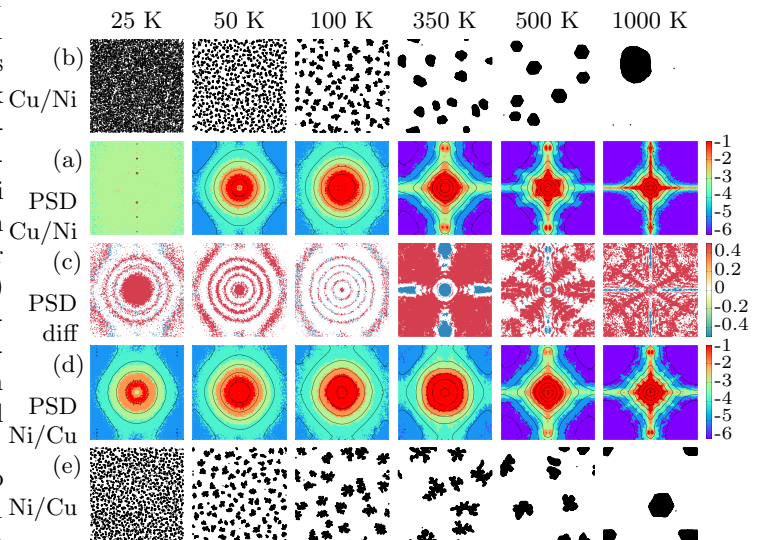


Figure 6: (b),(e) Surface morphology for Cu/Ni(111) and Ni/Cu(111), respectively, at  $\theta = 0.10$  and various temperatures (as indicated) with concerted island and multi-atom diffusion events activated. (a),(d) PSD maps for Cu/Ni(111) (a) and Ni/Cu(111) (d). (c) PSD difference maps.

At 25 K, where visual inspection is difficult, the PSD difference map displays several circular patterns, clearly deviating from random fluctuations around the 0 value (noise) and, thus, concluding that the two surfaces differ structurally. Note that perfect noise on the PSD difference

map is indicated by random blue/red/white values associated with positive/negative/zero fluctuations between the two maps. At 50 K, the PSD difference map is essentially the same as for 25 K, thus revealing structural differences. At 100 K, where both PSD maps are most similar, the difference map still shows circles. At the already considered temperature of 350 K, the Cu/Ni(111) map displays considerably higher values, except at the central and cross-like regions, where it is lower. At 500 K, the PSD difference map still reveals a strong structural mismatch. Here, the Cu/Ni(111) islands are almost hexagonal while the Ni/Cu(111) islands still remain amorphous. At the highest considered temperature (1000 K), both islands are compact. However, the shape for Cu/Ni(111) resembles a circle while that for Ni/Cu(111) approaches a hexagon; the PSD map for Cu/Ni(111) is mostly higher than that for Ni/Cu(111), with significantly lower values at the center and at four elongated horizontal/vertical regions. Overall, comparing the two systems at the same temperature and coverage, we conclude that they display different island densities and morphologies.

### 3.3. Total rate

In addition to the differences in the island density and morphology, also the average total rate per site,  $R = N/\tau$  (equation 21), differs between the two systems. This is shown in the Arrhenius plot of figure 7a for  $\theta = 0.10$  and  $T = 23 - 1000$  K, while the case for  $\theta = 0.01$  is shown in figure 7b and many other coverage values are considered in figures B1 and B2 of the appendix. These figures also display the average total rate per site determined using equation 24,  $R = \sum_{\alpha \in \{e\}} M_\alpha k_\alpha$ , demonstrating that both equations 21 and 24 provide equivalent descriptions of the same quantity. In addition, the figures also show the average total diffusion rate per site,  $R_d = N_d/\tau (= \sum_{\alpha \in \{h\}} M_\alpha k_\alpha)$  for the two systems and the average total adsorption rate per site,  $R_a = N_a/\tau$ , which is identical for both systems and independent of temperature, only depending on coverage:  $R_a = M_a k_a = (1 - \theta)F$ .

Regarding figure 7a, the total rate is much higher in the Ni/Cu(111) system, specially at low temperatures (e.g. region C). Since adsorption is identical in both systems and remains quite low, the difference in their total rate is primarily due to the total diffusion rate, which is higher for Ni/Cu(111). Nevertheless, in the Cu/Ni(111) system adsorption plays an important role at the lowest temperatures (region C), where it provides the largest contribution to the total rate, significantly over the total diffusion rate. In fact, the adsorption rate ( $1.5 \times 10^4$  Hz) is higher than the monomer diffusion rate at 25 K ( $3.3 \times 10^2$  Hz for a diffusion barrier of 52 meV). This behaviour is noticeable until about 32 K (the frontier between regions B and C), above which the total rate is essentially dominated by the total diffusion rate, as for the Ni/Cu(111) over the whole considered range of temperature.

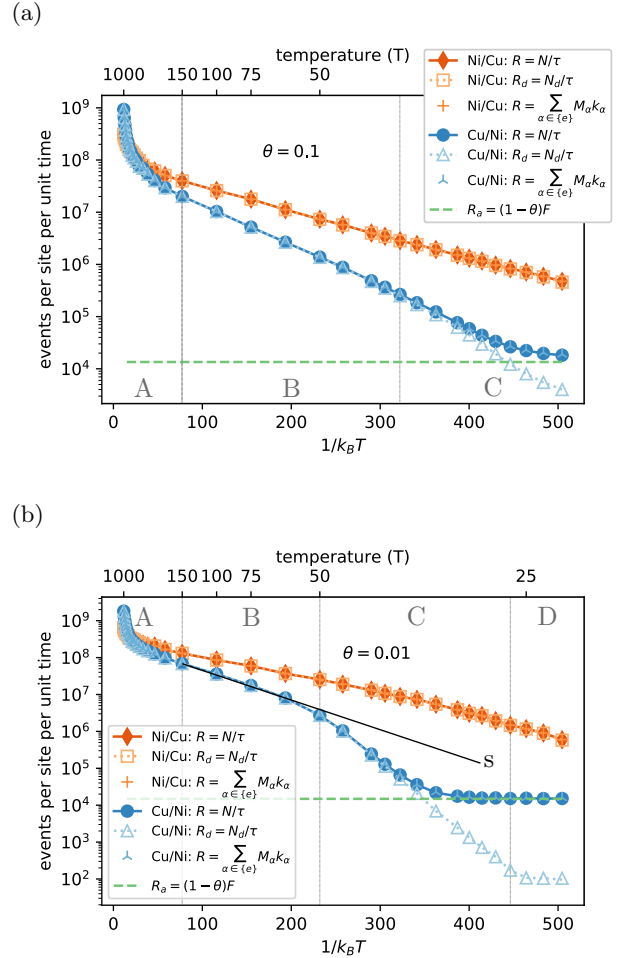


Figure 7: Average total rates per site for diffusion ( $R_h$ ), adsorption ( $R_a$ ) and all events ( $R = R_h + R_a$ ) for Cu/Ni(111) and Ni/Cu(111), as indicated, (a) at 10 % coverage and (b) at 1 % coverage.

At lower coverage, more complex behaviour is observed at low temperatures, as shown in regions C and D of figure 7b, especially in the case of  $R_d$  for Cu/Ni(111). As shown in section 3.4 below, the diffusivity in this case ( $R_d$  for Cu/Ni(111)) is dominated by non-concerted dimer diffusion in regions C and D and it is ruled by monomer diffusion in region B. In region A, monomer diffusion is complemented by perimeter diffusion and both concerted and non-concerted dimer diffusion, in addition to other secondary events. Although non-concerted dimer diffusion dominates in both regions C and D, it has not yet really been activated in region D. The behaviour for the total rate  $R$  of Cu/Ni(111) is similar to that of  $R_d$ , but  $R$  remains higher than  $R_d$  at low temperatures due to the larger value of the total adsorption rate ( $R_a$ ). Finally, the trend for Ni/Cu(111) in figure 7b is similar, but displaced towards lower temperatures.



### 3.4. Activation Energy

For the Arrhenius plot in figure 7a, the slope of  $R$  vs  $\beta$  is the apparent activation energy,  $E_{app}^R$ , which is shown in figure 8a for Ni/Cu(111) and figure 8b for Cu/Ni(111). While these plots correspond to  $\theta = 0.10$  and  $T = 23$ –1000 K, similar results for additional coverage values are shown in figures B5 and B6 of the appendix. In each plot, we show two temperature regions: (I)  $1000 \geq T > 150$  K, and (II)  $150 \geq T \geq 23$  K, with the low temperature region displayed in a magnified view. In addition, each region shows two alternative expressions for the apparent activation energy, namely,  $E_{app}^R = -\frac{\partial \log R}{\partial \beta}$  with  $R = N/\tau$  (equations 26 and 21) and  $E_{app}^{R,*} = \sum_{\alpha \in \{e\}} \epsilon_{\alpha}^R$  with  $\epsilon_{\alpha}^R = \omega_{\alpha}^R(E_{\alpha}^k + E_{\alpha}^M)$  (equation 29). The former ( $E_{app}^R$  in the plots) is obtained numerically by using finite central differences of  $\log R$  and  $\beta$ . The latter ( $\sum_{\alpha \in \{e\}} \epsilon_{\alpha}^R$  in the plots) is obtained from the rate of every event type,  $k_{\alpha}$ , and the corresponding multiplicity,  $M_{\alpha}$ , in order to determine the probability of every event type,  $\omega_{\alpha}^R$  (equation 25), as well as by summing the energy barrier,  $E_{\alpha}^k$ , and the configurational contribution,  $E_{\alpha}^M = -\frac{\partial \log M_{\alpha}}{\partial \beta}$ , calculated by finite differences as well. In addition, each plot shows the absolute error between the two measures,  $|E_{app}^R - \sum_{\alpha \in \{e\}} \epsilon_{\alpha}^R|$ , which remains smaller than 6.65 meV for Ni/Cu(111) and 3.12 meV for Cu/Ni(111), with a mean value of 0.49 meV for Ni/Cu(111) and 0.51 meV for Cu/Ni(111). The maximum error is typically due to the finite difference estimate of the slope (not the multiplicity based formula) and it usually occurs at the highest/lowest temperature or when  $\log R$  fluctuates with respect to the previous temperature. Thus, figures 8a and 8b show that equation 29 accurately explains the values observed for the apparent activation energy.

Next, we analyse the different contributions to the apparent activation energy. Before that, however, it is useful to note that, for Ni/Cu(111) in figure 8a, the apparent activation energy of the total rate,  $E_{app}^R$ , is also the apparent activation energy of the total diffusion rate,  $E_{app}^{R_d} = E_{app}^R$ , since  $R = R_d$  in this system (see figure 7a). In turn, based on equation 6, the apparent activation energy of the diffusivity is:  $E_{app}^{D_T} \approx E_{app}^{R_d} = E_{app}^R$ , since the contribution from the correlation factor,  $E^{f_T} = -\frac{\partial \log f_T}{\partial \beta}$ , is very small [27].

Since the apparent activation energy is constant ( $\approx 10$  meV) in region II of figure 8a for Ni/Cu(111), traditionally one would be tempted to conclude that there is a single rate-controlling event in this temperature range. However, 10 meV does not correspond to any of the energy barriers included in the system. In fact, the multiplicity analysis based on equation 29,  $E_{app}^R = \sum_{\alpha \in \{e\}} \epsilon_{\alpha}^R = \sum_{\alpha \in \{e\}} \omega_{\alpha}^R(E_{\alpha}^k + E_{\alpha}^M)$ , shows that there are three main contributing events in this region, namely, monomer diffusion ( $D[0,0] \rightarrow [0,0]$ , with  $E_{D[0,0] \rightarrow [0,0]}^k = 31$  meV), non-concerted dimer diffusion ( $D[1,0] \rightarrow [1,0]$ , with  $E_{D[1,0] \rightarrow [1,0]}^k = 16$  meV), and concerted dimer diffusion ( $I2$ , with  $E_{I2}^k = 21$  meV). The major contribution shifts from (non-concerted

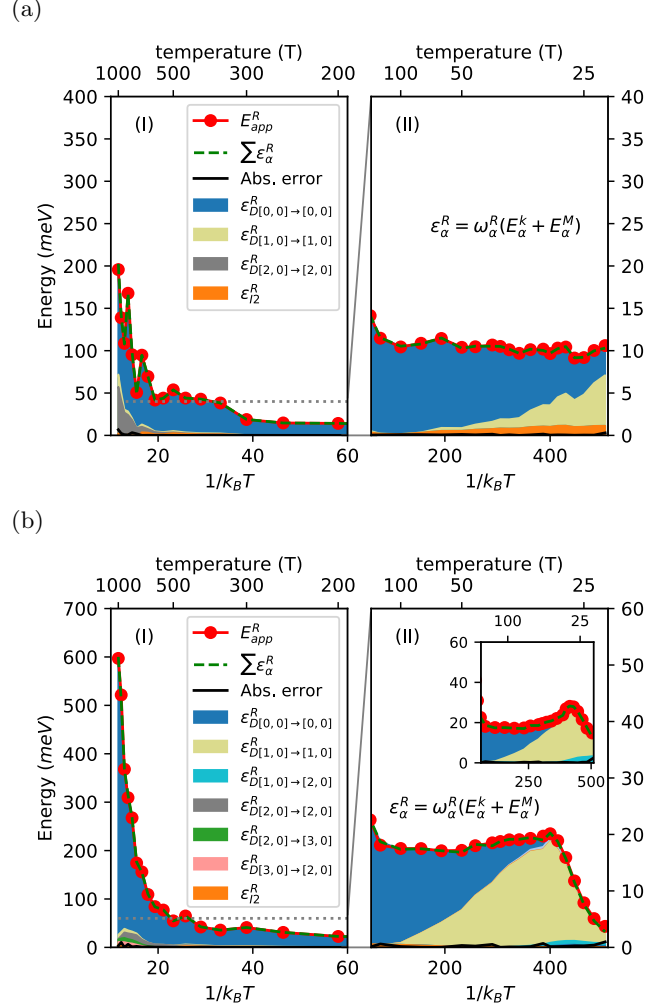


Figure 8: Temperature dependence of the apparent activation energy of the average total rate per site ( $E_{app}^R$ ) at  $\theta = 0.10$  for (a) Ni/Cu(111) and (b) Cu/Ni(111).  $E_{app}^R$  is described well by  $\sum_{\alpha \in \{e\}} \epsilon_{\alpha}^R$ , where  $\epsilon_{\alpha}^R = \omega_{\alpha}^R(E_{\alpha}^k + E_{\alpha}^M)$ . The absolute error  $|E_{app}^R - \sum_{\alpha \in \{e\}} \epsilon_{\alpha}^R|$  is also plotted.

+ concerted) dimer diffusion at the lowest temperatures (where the chance to form dimers is high) towards monomer diffusion at the highest temperatures in this range (where recently adsorbed monomers have a larger chance to reach an island than to form a dimer). Note that the shift is mostly due to the change in the event probabilities,  $\omega_{\alpha}^R$ , with temperature for those three particular event types, as shown in figure 9a. In addition, the configurational contributions to the apparent energy for the three event types,  $E_{D[0,0] \rightarrow [0,0]}^M$ ,  $E_{D[1,0] \rightarrow [1,0]}^M$  and  $E_{I2}^M$ , are negative in this case, thus leading to a value of the apparent activation energy ( $\approx 10$  meV) that is significantly smaller than any of the three energy barriers (31, 16 and 21 meV).

For the lowest temperatures ( $T < 60$  K), figure 9a shows that several additional event types have appreciable roles, with probabilities larger than 0.1% and up to about 3%. This includes adsorption (no energy barrier),

monomer attachment to the islands ( $D[0,0] \rightarrow [1,0]$  and  $D[0,0] \rightarrow [2,0]$ , with energy barriers of 28 and 15 meV, respectively) and perimeter adatom stabilization ( $D[1,0] \rightarrow [2,0]$ , 14 meV;  $D[1,0] \rightarrow [2,2]$ , 0 meV; and  $D[1,0] \rightarrow [3,0]$ , 1 meV). Furthermore, concerted dimer diffusion ( $I2$ , with  $E_{I2}^k = 21$  meV) has an appreciable role over the complete temperature range, with an event probability of 8-10% up to about 50 K, and remaining active at higher temperatures ( $\geq 1\%$ ). Finally, at the highest temperatures, edge diffusion ( $D[2,0] \rightarrow [2,0]$ , with  $E_{D[2,0] \rightarrow [2,0]}^k = 364$  meV), trimer diffusion ( $I3$ , with  $E_{I3}^k = 148$  meV) and a few other processes become relevant, with event probabilities larger than 0.1%.

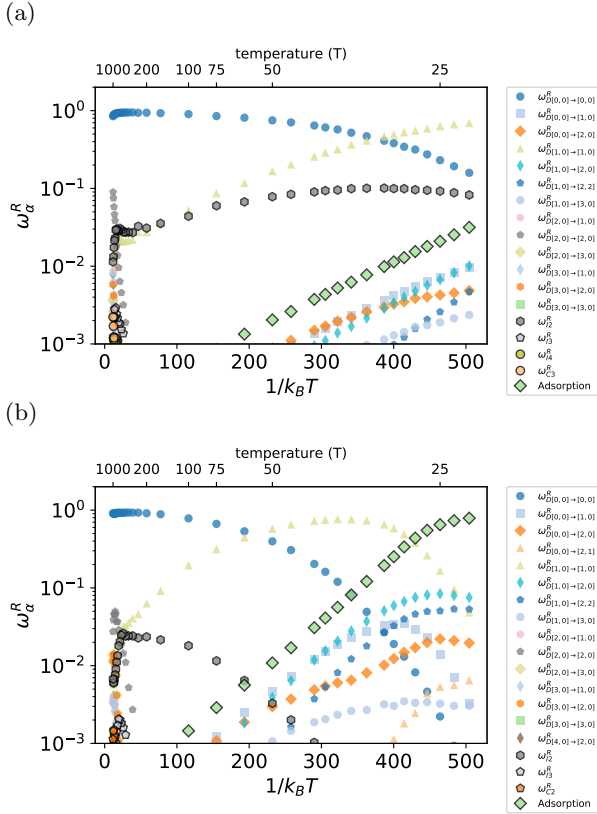


Figure 9: Temperature dependence of the event probabilities,  $w_\alpha^R$ , at  $\theta = 0.10$  for (a) Ni/Cu(111) and (b) Cu/Ni(111). Only those events whose probability is higher than  $10^{-3}$  are shown.

Here, the energy barrier for non-concerted dimer diffusion (16 meV) is smaller than that for concerted dimer diffusion (21 meV) and, thus, non-concerted diffusion has a larger rate, especially at low temperatures (e.g.  $k_{D[1,0] \rightarrow [1,0]} = 3.1 \times 10^9$  Hz and  $k_{I2} = 2.5 \times 10^8$  Hz at 23 K). On the other hand, the multiplicities of the two event types are similar, with  $M_{D[1,0] \rightarrow [1,0]} = 4n_2$  (where  $n_2$  is the density of dimers and both atoms may hop in two directions while remaining attached to the other, thus leading to a multiplicity of  $2 \cdot 2 = 4$  per dimer) while  $M_{I2} = 6n_2$  (since there are six hop directions in the triangular lattice). Thus, comparing the total rates per site for both events,  $4n_2 k_{D[1,0] \rightarrow [1,0]}$  and  $6n_2 k_{I2}$ , non-concerted dimer diffusion occurs more of-

ten at low temperatures. However, at high temperatures the two rates become very similar and concerted dimer diffusion occurs more frequently due to the slightly larger multiplicity. See figure B4 in the appendix for further proof. Based on this example, we believe that there may be systems where concerted dimer diffusion dominates over non-concerted diffusion in a wide range of temperature.

For Cu/Ni(111) in figure 8b, the situation is very similar, except for the fact that  $E_{app}^R$  approaches zero at the low temperature end. In this region, the total rate is dominated by adsorption,  $R = R_a = M_a k_a$  (see figure 7a), with both the adsorption rate,  $k_a = F$ , and the multiplicity,  $M_a = 1 - \theta$ , being temperature independent. Thus,  $\epsilon_a^R = \omega_a^R (E_a^k + E_a^M) = 0$ , because  $E_a^k = E_a^M = 0$  even though  $w_a^R \approx 1$  (see figure 9b).

The insert in figure 8b for  $\theta = 0.1$  displays the apparent activation energy of the total diffusion rate per site,  $E_{app}^R$ , characterised by a weak maximum in the range 23-50 K, which is clearly assigned to the temperature dependence of  $\epsilon_{D[1,0] \rightarrow [1,0]}^R$  (non-concerted dimer diffusion). Note that a similar maximum is observed in the insert of figure B5 for  $\theta = 0.01$  in the appendix and it is also assigned to  $\epsilon_{D[1,0] \rightarrow [1,0]}^R$ . For such low temperatures, the quickly-diffusing dimers (through non-concerted diffusion) collide against the slowly-diffusing monomers (which essentially act as stationary obstacles). This generates both triangular (immobile) and chain-like (mobile) trimers, which are eventually compacted into the triangular (immobile) shape *via* perimeter adatom stabilization ( $D[1,0] \rightarrow [2,0]$  and  $D[1,0] \rightarrow [2,2]$ ). The maxima in  $\epsilon_{D[1,0] \rightarrow [1,0]}^R$  in the inserts of figure 8b for  $\theta = 0.1$  and figure B5 for  $\theta = 0.01$  correlate with the peaks in the probability of generating dimers,  $\omega_{D[0,0] \rightarrow [1,0]}^R$ , as shown in figure 9b for  $\theta = 0.1$  and figure B7 for  $\theta = 0.01$ , respectively. Thus, as the temperature is increased, a larger fraction of the monomers start diffusing and, as a result, there are less obstacles and a lower probability to form dimers. Consequently, the dominance by dimer diffusion gives away to the dominance by monomer diffusion.

According to figure 9b, the biggest difference with respect to Ni/Cu(111) at low temperature is the strong dominance by adsorption (no energy barrier), monomer attachment to the islands ( $D[0,0] \rightarrow [1,0]$  and  $D[0,0] \rightarrow [2,0]$ , with energy barriers of 35 and 31 meV, respectively) and stabilization of recently-attached monomers ( $D[1,0] \rightarrow [2,0]$ , 26 meV;  $D[1,0] \rightarrow [2,2]$ , 10 meV; and  $D[1,0] \rightarrow [3,0]$ , 10 meV). Note that, in the Cu/Ni(111) system, the role of concerted dimer diffusion ( $I2$ ) is less significant, achieving an event probability of between 0.1 and 2.8% at high temperatures. Similarly, at the highest considered temperatures, edge diffusion ( $D[2,0] \rightarrow [2,0]$ , with  $E_{D[2,0] \rightarrow [2,0]}^k = 268$  meV) becomes appreciable.

Further plots for the event probabilities as a function of temperature are shown for representative coverages in figures B7 and B8 of the appendix, for Cu/Ni(111) and for Ni/Cu(111), respectively. The trend at any coverage is

much equivalent to the picture just presented. In general, the Cu/Ni(111) system is dominated by monomer diffusion ( $D[0, 0] \rightarrow [0, 0]$ ) at high temperatures, non-concerted dimer diffusion ( $D[1, 0] \rightarrow [1, 0]$ ) at intermediate temperatures, and adsorption at low temperatures. At this end (low temperature), monomer attachment to the islands ( $D[0, 0] \rightarrow [1, 0]$ ,  $D[0, 0] \rightarrow [2, 0]$  and  $D[0, 0] \rightarrow [3, 0]$ ) and stabilisation of recently-attached monomers ( $D[1, 0] \rightarrow [2, 0]$ ,  $D[1, 0] \rightarrow [2, 2]$  and  $D[1, 0] \rightarrow [3, 0]$ ) are also relevant, becoming more important the lower the temperature and the higher the coverage, each one on a different scale. The same trend is valid for the Ni/Cu(111) system, although the importance of adsorption, monomer attachment and recently-attached-monomer stabilisation at low temperatures is less significant. In addition, concerted dimer diffusion has an appreciable role in this system at all coverages and over the whole range of temperature. For completeness, the event probabilities for the most relevant events are also shown as three-dimensional plots against coverage and inverse temperature in figures B9 and B10 of the appendix, for Cu/Ni(111) and for Ni/Cu(111), respectively.

#### 4. Conclusions

We perform kinetic Monte Carlo simulations of two-dimensional submonolayer growth at constant deposition flux, where the rate of interest—the tracer diffusivity—is shown to be proportional to the total diffusion rate,  $R_d = \sum_{\alpha \in \{d\}} M_\alpha k_\alpha$ , and closely related to the total rate,  $R = \sum_{\alpha \in \{e\}} M_\alpha k_\alpha$ . This means that the growth process depends on both the rates of the distinct events,  $k_\alpha$ , and their multiplicities,  $M_\alpha$ , i.e. the numbers of locations where each event  $\alpha$  can be performed in a given snapshot of the surface. Based on this, we focus on the study of two specific metallic heteroepitaxial systems, namely, Cu on Ni(111) and Ni on Cu(111), as a function of coverage and temperature while including a large variety of single-atom, multi-atom and complete-island diffusion events. The interaction between the atoms is described with a many body semi empirical embedded atom model and the drag method is used to calculate the energy barriers. The two systems are compared in terms of their temperature-dependent morphology, island density and diffusivity, through the total rates,  $R_d$  and  $R$ , including their apparent activation energies,  $E_{app}^R$  and  $E_{app}^{R_d}$ .

The use of the multiplicities allows describing the probability of every event with respect to all others. As a result, we conclude that, at low temperature, the diffusivity is dominated by dimer diffusion, which is split between non-concerted dimer diffusion and concerted dimer diffusion. At medium temperature, it is controlled by monomer diffusion and, at high temperature, it is due to a mixture of monomer diffusion, perimeter diffusion and concerted dimer/trimer diffusion. Thus, this work shows the importance of some concerted diffusion events in 2D submonolayer epitaxial growth. Although concerted diffusion has

a substantial role in one of the two analysed systems, it is to be expected that concerted motion may be even more important in other systems, including the relatively unexplored area of on-surface synthesis.

Most importantly, the use of the multiplicities enables formulating the apparent activation energy as a weighted average, where the weights are identified as the probabilities of the different events and the actual energy contribution for every event contains both the traditional energy barrier and an additional unbounded configurational term, directly related to the temperature dependence of its multiplicity. Since the leading event in the weighted average may easily change with the growth conditions and the configurational terms may vary widely, we show that a constant value of the apparent activation energy can be obtained even if control shifts from one elementary reaction to another. This means that the traditional assignment of a constant apparent activation energy to an underlying rate determining step is not the only possibility and, thus, it is not necessarily valid during epitaxial growth.

The study demonstrates that the multiplicity analysis can be applied for systems with hundreds of distinct events, showing that eventually a few of them dominate the growth process. In the future, the addition of self-learning KMC (SLKMC) techniques should enable finding and executing new diffusion events, for any type of single-atom and multi-atom event. The present work opens the door to include the multiplicity analysis into the existing SLKMC methods.

#### Acknowledgements

We acknowledge support by the project “Connecting Mesoscale Dynamics of Metallic Films on Semiconductors to Nanoscale Phenomena,” by the US National Science Foundation, by the Basque Departamento de Educacion, UPV/EHU (Grant No. IT-756-13), and the 2015/01 contract by the DIPC. The KMC calculations were performed on the ATLAS supercomputer in the DIPC. We would like to acknowledge STOKES advanced computing center at the University of Central Florida for resources to calculate barriers of processes. We are thankful to Dr. N. Ferrando from Universitat Politècnica de València, for the main development of the PSD tool as well as an initial implementation of the “Morphokinetics” KMC code.

#### References

- [1] H. Zhang, Ultrathin two-dimensional nanomaterials, *ACS Nano* 9 (10) (2015) 9451–9469, pMID: 26407037. [arXiv:https://doi.org/10.1021/acsnano.5b05040](https://arxiv.org/abs/https://doi.org/10.1021/acsnano.5b05040), doi:10.1021/acsnano.5b05040. URL <https://doi.org/10.1021/acsnano.5b05040>
- [2] Z. Lin, A. McCreary, N. Briggs, S. Subramanian, K. Zhang, Y. Sun, X. Li, N. J. Borys, H. Yuan, S. K. Fullerton-Shirey, A. Chernikov, H. Zhao, S. McDonnell, A. M. Lindenberg,

- K. Xiao, B. J. LeRoy, M. Drndi, J. C. M. Hwang, J. Park, Manish Chhowalla, R. E. Schaak, A. Javey, M. C. Hersam, J. Robinson, M. Terrones, 2d materials advances: from large scale synthesis and controlled heterostructures to improved characterization techniques, defects and applications, *2D Materials* 3 (4) (2016) 042001. doi:10.1088/2053-1583/3/4/042001.  
URL <http://stacks.iop.org/2053-1583/3/i=4/a=042001>
- [3] Q. Shen, H.-Y. Gao, H. Fuchs, Frontiers of on-surface synthesis: From principles to applications, *Nano Today* 13 (2017) 77–96. doi:10.1016/j.nantod.2017.02.007.  
URL <http://www.sciencedirect.com/science/article/pii/S174801321630531X>
- [4] S. Zhuikov, T. Kawaguchi, Z. Hai, M. K. Akbari, P. M. Heynderickx, Interfacial engineering of two-dimensional nanostructured materials by atomic layer deposition, *Applied Surface Science* 392 (2017) 231–243. doi:https://doi.org/10.1016/j.apsusc.2016.09.040.  
URL <http://www.sciencedirect.com/science/article/pii/S0169433216319080>
- [5] K. S. Novoselov, A. K. Geim, S. V. Morozov, D. Jiang, Y. Zhang, S. V. Dubonos, I. V. Grigorieva, A. A. Firsov, Electric field effect in atomically thin carbon films, *Science* 306 (5696) (2004) 666–669. arXiv: <http://science.sciencemag.org/content/306/5696/666.full.pdf>, doi:10.1126/science.1102896.  
URL <http://science.sciencemag.org/content/306/5696/666>
- [6] M. E. Dvila, L. Xian, S. Cahangirov, A. Rubio, G. L. Lay, Germanene: a novel two-dimensional germanium allotrope akin to graphene and silicene, *New Journal of Physics* 16 (9) (2014) 095002.  
URL <http://stacks.iop.org/1367-2630/16/i=9/a=095002>
- [7] C. Grazianetti, E. Cinquanta, A. Molle, Two-dimensional silicene: the advent of silicene, *2D Materials* 3 (1) (2016) 012001. doi:10.1088/2053-1583/3/1/012001.  
URL <http://stacks.iop.org/2053-1583/3/i=1/a=012001>
- [8] K. S. Kim, Y. Zhao, H. Jang, S. Y. Lee, J. M. Kim, K. S. Kim, J.-H. Ahn, P. Kim, J.-Y. Choi, B. H. Hong, Large-scale pattern growth of graphene films for stretchable transparent electrodes, *Nature* 457 (7230) (2009) 706–710. doi:10.1038/nature07719.  
URL <https://www.nature.com/articles/nature07719>
- [9] M. Huang, M. Biswal, H. J. Park, S. Jin, D. Qu, S. Hong, Z. Zhu, L. Qiu, D. Luo, X. Liu, Z. Yang, Z. Liu, Y. Huang, H. Lim, W. J. Yoo, F. Ding, Y. Wang, Z. Lee, R. S. Ruoff, Highly Oriented Monolayer Graphene Grown on a Cu/Ni(111) Alloy Foil, *ACS Nano* 12 (6) (2018) 6117–6127. doi:10.1021/acsnano.8b02444.  
URL <http://pubs.acs.org/doi/10.1021/acsnano.8b02444>
- [10] Y. Takesaki, K. Kawahara, H. Hibino, S. Okada, M. Tsuji, H. Ago, Highly Uniform Bilayer Graphene on Epitaxial CuNi(111) Alloy, *Chem. Mater.* 28 (13) (2016) 4583–4592. doi:10.1021/acs.chemmater.6b01137.  
URL <http://pubs.acs.org/doi/10.1021/acs.chemmater.6b01137>
- [11] C.-M. Seah, S.-P. Chai, A. R. Mohamed, Mechanisms of graphene growth by chemical vapour deposition on transition metals, *Carbon* 70 (2014) 1–21. doi:10.1016/j.carbon.2013.12.073.  
URL <http://www.sciencedirect.com/science/article/pii/S0008622313012281>
- [12] J. Tian, B. Hu, Z. Wei, Y. Jin, Z. Luo, M. Xia, Q. Pan, Y. Liu, Surface structure deduced differences of copper foil and film for graphene CVD growth, *Applied Surface Science* 300 (2014) 73–79. doi:10.1016/j.apsusc.2014.02.004.  
URL <http://www.sciencedirect.com/science/article/pii/S0169433214002888>
- [13] B. Huet, J.-P. Raskin, Role of Cu foil in-situ annealing in controlling the size and thickness of CVD graphene domains, *Carbon* 129 (2018) 270–280. doi:10.1016/j.carbon.2017.12.043.  
URL <http://www.sciencedirect.com/science/article/pii/S0008622317312769>
- [14] N. S. Mueller, A. J. Morfa, D. Abou-Ras, V. Oddone, T. Ciuk, M. Giersig, Growing graphene on polycrystalline copper foils by ultra-high vacuum chemical vapor deposition, *Carbon* 78 (2014) 347–355. doi:10.1016/j.carbon.2014.07.011.  
URL <http://www.sciencedirect.com/science/article/pii/S0008622314006344>
- [15] W. Liu, H. Li, C. Xu, Y. Khatami, K. Banerjee, Synthesis of high-quality monolayer and bilayer graphene on copper using chemical vapor deposition, *Carbon* 49 (13) (2011) 4122–4130. doi:10.1016/j.carbon.2011.05.047.  
URL <http://www.sciencedirect.com/science/article/pii/S0008622311004106>
- [16] C. Davisson, L. H. Germer, The Scattering of Electrons by a Single Crystal of Nickel, *Nature* 119 (2998) (1927) 558–560. doi:10.1038/119558a0.  
URL <https://www.nature.com/articles/119558a0>
- [17] C. Davisson, L. H. Germer, Diffraction of Electrons by a Crystal of Nickel, *Physical Review* 30 (6) (1927) 705–740. doi:10.1103/PhysRev.30.705.  
URL <https://link.aps.org/doi/10.1103/PhysRev.30.705>
- [18] H. Viefhaus, Low-energy electron diffraction. Von M. A. Van Hove, W. H. Weinberg und C.-M. Chn. Springer-Verlag Berlin - Heidelberg - New York - London - Paris -Tokyo 1986. XVII, 603 S., 213 Abb., DM 124,-.ISBN 3-540-16262-3, *Materials and Corrosion* 38 (7) (1987) 404–404. doi:10.1002/maco.19870380711.  
URL <https://onlinelibrary.wiley.com/doi/abs/10.1002/maco.19870380711>
- [19] E. W. Mller, K. Bahadur, Field Ionization of Gases at a Metal Surface and the Resolution of the Field Ion Microscope, *Physical Review* 102 (3) (1956) 624–631. doi:10.1103/PhysRev.102.624.  
URL <https://link.aps.org/doi/10.1103/PhysRev.102.624>
- [20] E. W. Mller, Resolution of the Atomic Structure of a Metal Surface by the Field Ion Microscope, *Journal of Applied Physics* 27 (5) (1956) 474–476. doi:10.1063/1.1722406.  
URL <https://aip.scitation.org/doi/abs/10.1063/1.1722406>
- [21] G. Binnig, H. Rohrer, Scanning tunneling microscopy, *Surface Science* 126 (1) (1983) 236–244. doi:10.1016/0039-6028(83)90716-1.  
URL <http://www.sciencedirect.com/science/article/pii/0039602883907161>
- [22] G. Antczak, G. Ehrlich, Surface diffusion: metals, metal atoms, and clusters, Cambridge University Press, 2010.
- [23] N. Knorr, H. Brune, M. Epple, A. Hirstein, M. A. Schneider, K. Kern, Long-range adsorbate interactions mediated by a two-dimensional electron gas, *Physical Review B* 65 (11) (2002) 115420. doi:10.1103/PhysRevB.65.115420.  
URL <https://link.aps.org/doi/10.1103/PhysRevB.65.115420>
- [24] J. Repp, F. Moresco, G. Meyer, K.-H. Rieder, P. Hyldgaard, M. Persson, Substrate Mediated Long-Range Oscillatory Interaction between Adatoms: Cu  $\beta$ /Cu(111), *Physical Review Letters* 85 (14) (2000) 2981–2984. doi:10.1103/PhysRevLett.85.2981.  
URL <https://link.aps.org/doi/10.1103/PhysRevLett.85.2981>
- [25] J. Repp, G. Meyer, K.-H. Rieder, P. Hyldgaard, Site Determination and Thermally Assisted Tunneling in Homogenous Nucleation, *Physical Review Letters* 91 (20) (2003) 206102. doi:10.1103/PhysRevLett.91.206102.  
URL <https://link.aps.org/doi/10.1103/PhysRevLett.91.206102>
- [26] K. Morgenstern, K.-F. Braun, K.-H. Rieder, Direct Imaging of Cu Dimer Formation, Motion, and Interaction with Cu Atoms on Ag(111), *Physical Review Letters* 93 (5) (2004) 056102. doi:10.1103/PhysRevLett.93.056102.  
URL <https://link.aps.org/doi/10.1103/PhysRevLett.93.056102>
- [27] M. A. Gosálvez, J. Alberdi-Rodríguez, Activation energy in monolayer growth of two-dimensional materials, *J. Phys. Chem. C* 121 (37) (2017) 20315–20322. doi:10.1021/acs.jpcc.7b05794.  
URL <https://doi.org/10.1021/acs.jpcc.7b05794>

- [28] S. R. Acharya, S. I. Shah, T. S. Rahman, Diffusion of small Cu islands on the Ni (111) surface: A self-learning kinetic Monte Carlo study, *Surf. Sci.* 662 (2017) 42–58. doi:<https://doi.org/10.1016/j.susc.2017.03.012>. URL <http://www.sciencedirect.com/science/article/pii/S0039602816302503>
- [29] B. Onat, S. Durukanolu, An optimized interatomic potential for CuNi alloys with the embedded-atom method, *J. Phys.: Condens. Matter* 26 (3) (2014) 035404. doi:10.1088/0953-8984/26/3/035404. URL <http://stacks.iop.org/0953-8984/26/i=3/a=035404?key=crossref.91b4aac7cb0079f63d5e0fa001ef708>
- [30] H. Koschel, G. Held, P. Trischberger, W. Widdra, U. Birkenheuer, H.-P. Steinrück, Electronic properties of a pseudomorphic Cu-layer on Ni(111), *Appl. Surf. Sci.* 142 (1-4) (1999) 18–22. doi:[https://doi.org/10.1016/S0169-4332\(98\)00741-7](https://doi.org/10.1016/S0169-4332(98)00741-7). URL <http://www.sciencedirect.com/science/article/pii/S0169433298007417>
- [31] H. Koschel, G. Held, H. P. Steinrück, The growth of thin Cu layers on Ni(111) studied by CO titration and photoelectron spectroscopy, *Surf. Sci.* 453 (1) (2000) 201–213. doi:10.1016/S0039-6028(00)00349-6. URL <http://www.sciencedirect.com/science/article/pii/S0039602800003496>
- [32] C. Boeglin, S. Stanescu, S. Cherifi, J. P. Deville, P. Ohresser, A. Barbier, N. B. Brookes, High dipolar magnetic moment observed on Ni/Cu(111) nanostructures by magnetic circular X-ray dichroism, *Surf. Sci.* 507-510 (2002) 522–529. doi:10.1016/S0039-6028(02)01303-1. URL <http://www.sciencedirect.com/science/article/pii/S0039602802013031>
- [33] S. Pons, P. Mallet, L. Magaud, J. Y. Veuillen, Spontaneous evolution of the Ni/Cu(111) interface at 300 K, *Surf. Sci.* 511 (1) (2002) 449–458. doi:10.1016/S0039-6028(02)01541-8. URL <http://www.sciencedirect.com/science/article/pii/S0039602802015418>
- [34] M. Mulazzi, S. Stanescu, J. Fujii, I. Vobornik, C. Boeglin, R. Belkhou, G. Rossi, A. Barbier, Structural and electronic properties of thin Ni layers on Cu(111) as investigated by ARPES, STM and GXD, *Surf. Sci.* 600 (18) (2006) 3938–3942. doi:10.1016/j.susc.2006.01.104. URL <http://linkinghub.elsevier.com/retrieve/pii/S0039602806004304>
- [35] A. P. J. Jansen, An introduction to kinetic Monte Carlo simulations of surface reactions, 1st Edition, no. 856 in *Lecture notes in physics*, Springer, New York, 2012. doi:10.1007/978-3-642-29488-4. URL <https://link.springer.com/book/10.1007/978-3-642-29488-4>
- [36] D. T. Gillespie, Exact stochastic simulation of coupled chemical reactions, *The Journal of Physical Chemistry* 81 (25) (1977) 2340–2361. doi:10.1021/j100540a008. URL <https://doi.org/10.1021/j100540a008>
- [37] S. Foiles, M. Baskes, M. S. Daw, Embedded-atom-method functions for the fcc metals Cu, Ag, Au, Ni, Pd, Pt, and their alloys, *Phys. Rev. B* 33 (12) (1986) 7983. doi:10.1103/PhysRevB.33.7983. URL <https://link.aps.org/doi/10.1103/PhysRevB.33.7983>
- [38] O. Trushin, A. Karim, A. Kara, T. S. Rahman, Self-learning kinetic Monte Carlo method: application to Cu (111), *Phys. Rev. B* 72 (11) (2005) 115401. doi:10.1103/PhysRevB.72.115401. URL <https://link.aps.org/doi/10.1103/PhysRevB.72.115401>
- [39] S. R. Acharya, T. S. Rahman, Toward multiscale modeling of thin-film growth processes using SLKMC, *J. Mater. Res.* 33 (6) (2018) 709–719. doi:10.1557/jmr.2018.44.
- [40] B. Persson, O. Albohr, U. Tartaglino, A. Volokitin, E. Tosatti, On the nature of surface roughness with application to contact mechanics, sealing, rubber friction and adhesion, *J. Phys.: Condens. Matter* 17 (1) (2005) R1. doi:10.1088/0953-8984/17/1/R01. URL <http://stacks.iop.org/0953-8984/17/i=1/a=R01>
- [41] J. M. Elson, J. M. Bennett, Calculation of the power spectral density from surface profile data, *Appl. Opt.* 34 (1) (1995) 201–208. doi:10.1364/AO.34.000201. URL <http://ao.osa.org/abstract.cfm?URI=ao-34-1-201>
- [42] Á. Czifra, Sensitivity of power spectral density (psd) analysis for measuring conditions, in: I. Rudas, J. Fodor, J. Kacprzyk (Eds.), *Towards Intelligent Engineering and Information Technology*, Springer, 2009, pp. 505–517. doi:10.1007/978-3-642-03737-5\_36.
- [43] N. Ferrando, M. A. Gosálvez, A. Ayuela, Evolutionary kinetic Monte Carlo: Atomistic rates of surface-mediated processes from surface morphologies, *J. Phys. Chem. C* 118 (22) (2014) 11636–11648. arXiv:<http://dx.doi.org/10.1021/jp409812x>, doi:10.1021/jp409812x. URL <http://dx.doi.org/10.1021/jp409812x>
- [44] S. C. Wang, U. Kürpick, G. Ehrlich, Surface diffusion of compact and other clusters: Ir<sub>n</sub> on Ir(111), *Phys. Rev. Lett.* 81 (1998) 4923–4926. doi:10.1103/PhysRevLett.81.4923. URL <https://link.aps.org/doi/10.1103/PhysRevLett.81.4923>
- [45] D. C. Schlößer, K. Morgenstern, L. K. Verheij, G. Rosenfeld, F. Besenbacher, G. Comsa, Kinetics of island diffusion on Cu (111) and Ag (111) studied with variable-temperature STM, *Surf. Sci.* 465 (1-2) (2000) 19–39. doi:[https://doi.org/10.1016/S0039-6028\(00\)00682-8](https://doi.org/10.1016/S0039-6028(00)00682-8). URL <http://www.sciencedirect.com/science/article/pii/S0039602800006828>
- [46] G. Kellogg, Oscillatory behavior in the size dependence of cluster mobility on metal surfaces: Rh on Rh (100), *Phys. Rev. Lett.* 73 (13) (1994) 1833. doi:10.1103/PhysRevLett.73.1833. URL <https://link.aps.org/doi/10.1103/PhysRevLett.73.1833>
- [47] Z. Zhang, M. G. Lagally, Atomistic processes in the early stages of thin-film growth, *Science* 276 (5311) (1997) 377–383. doi:10.1126/science.276.5311.377. URL <http://science.sciencemag.org/content/276/5311/377>
- [48] S. Wang, G. Ehrlich, Diffusion of large surface clusters: direct observations on Ir (111), *Phys. Rev. Lett.* 79 (21) (1997) 4234. doi:10.1103/PhysRevLett.79.4234. URL <https://link.aps.org/doi/10.1103/PhysRevLett.79.4234>
- [49] H. H. Wu, A. Signor, D. R. Trinkle, Island shape controls magic-size effect for heteroepitaxial diffusion, *J. Appl. Phys.* 108 (2) (2010) 023521. doi:10.1063/1.3455848. URL <https://doi.org/10.1063/1.3455848>
- [50] A. Signor, H. H. Wu, D. R. Trinkle, Misfit-dislocation-mediated heteroepitaxial island diffusion, *Surf. Sci.* 604 (21-22) (2010) L67–L70. doi:<https://doi.org/10.1016/j.susc.2010.08.003>. URL <http://www.sciencedirect.com/science/article/pii/S0039602810003201>
- [51] S. Y. Kim, I.-H. Lee, S. Jun, Transition-pathway models of atomic diffusion on fcc metal surfaces. i. flat surfaces, *Phys. Rev. B* 76 (24) (2007) 245407. doi:10.1103/PhysRevB.76.245407. URL <https://link.aps.org/doi/10.1103/PhysRevB.76.245407>
- [52] J. A. Venables, G. D. T. Spiller, M. Hanbucken, Nucleation and growth of thin films, *Reports on Progress in Physics* 47 (4) (1984) 399. URL <http://stacks.iop.org/0034-4885/47/i=4/a=002>
- [53] J. G. Amar, F. Family, P.-M. Lam, Dynamic scaling of the island-size distribution and percolation in a model of submonolayer molecular-beam epitaxy, *Phys. Rev. B* 50 (1994) 8781–8797. doi:10.1103/PhysRevB.50.8781. URL <https://link.aps.org/doi/10.1103/PhysRevB.50.8781>
- [54] C. Ratsch, J. A. Venables, Nucleation theory and the early stages of thin film growth, *Journal of Vacuum Science & Technology A: Vacuum, Surfaces, and Films* 21 (5) (2003) S96–S109. arXiv:<http://dx.doi.org/10.1116/1.1600454>, doi:10.1116/1.1600454.



URL <http://dx.doi.org/10.1116/1.1600454>

- [55] M. Körner, M. Einax, P. Maass, Capture numbers and island size distributions in models of submonolayer surface growth, *Phys. Rev. B* 86 (2012) 085403. doi:10.1103/PhysRevB.86.085403.  
URL <https://link.aps.org/doi/10.1103/PhysRevB.86.085403>
- [56] M. A. Gosálvez, J. Alberdi-Rodriguez, A microscopic perspective on heterogeneous catalysis, ArXiv.  
URL [arXiv:1812.11398](https://arxiv.org/abs/1812.11398)[physics.chem-ph]
- [57] J. A. Venables, Nucleation calculations in a pair-binding model, *Phys. Rev. B* 36 (8) (1987) 4153–4162. doi:10.1103/PhysRevB.36.4153.  
URL <https://link.aps.org/doi/10.1103/PhysRevB.36.4153>

## A1. Diffusion events appendix

### A1.1. Single-atom available diffusion events

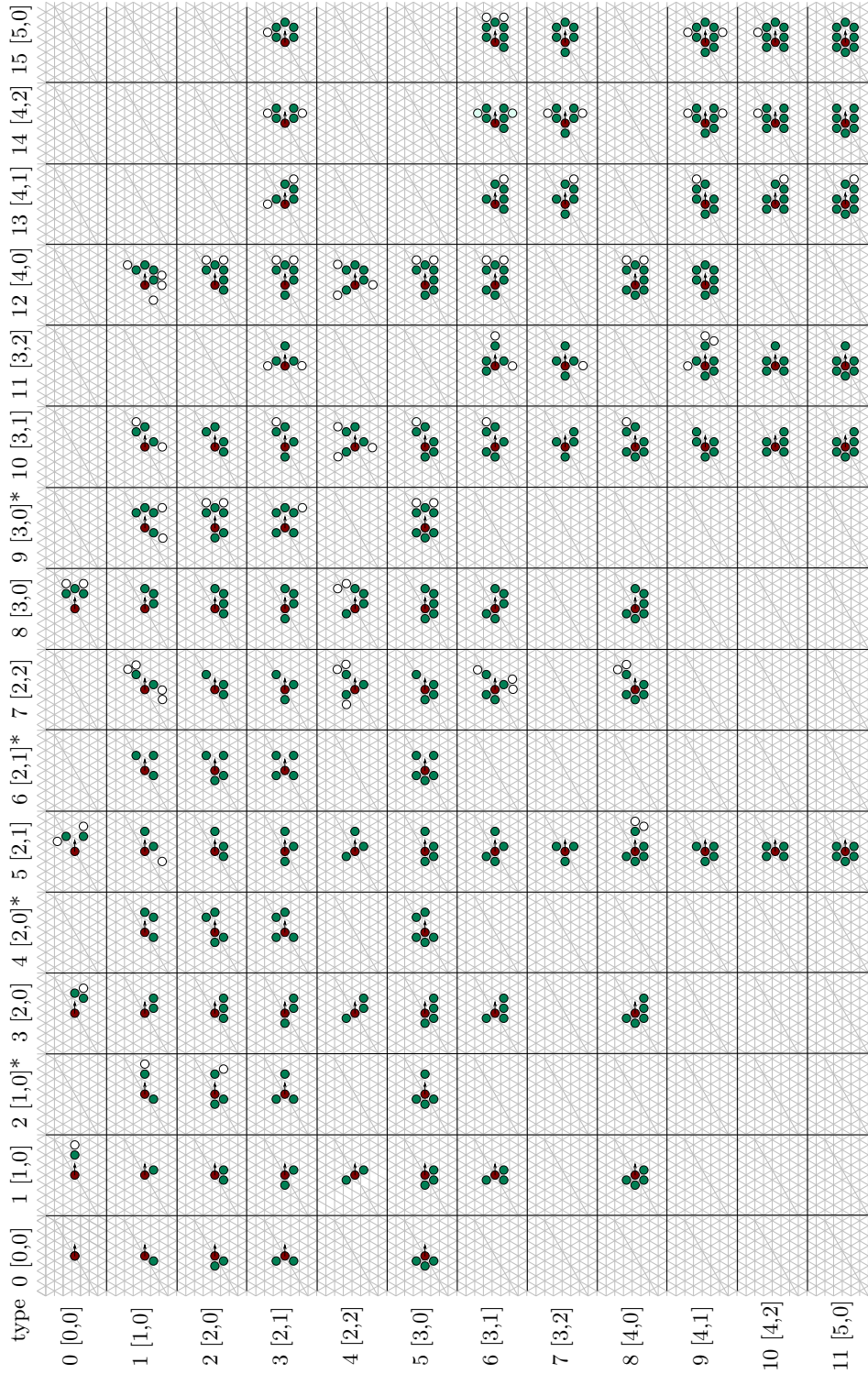


Figure A1: Complete table for all single atom events considered in this study. The red adatom is moved one position to the right. The green adatoms are nearest neighbours of the origin/destination sites. White adatoms have been used to stabilise the structures in EAM+drag. \* denotes detachment, where the destination site has no neighbours in common with the origin site. The table contains 107 single atom event types. Taking into account concerted island diffusion (7 types, figure 3a), multi-atom diffusion (4 types, figure 3b) and the adsorption event (1 unique event type), the KMC simulations use a total of 119 different event types.

A1.2. Activation energies for Cu/Ni and Ni/Cu

Table A1: Microscopic diffusion activation energy barriers (in eV) for Cu/Ni system.

| Type     | [class, subclass] |         | Single atom diffusion events |         |          |         |          |         |         |          |          |          |          |          |          |          |  |
|----------|-------------------|---------|------------------------------|---------|----------|---------|----------|---------|---------|----------|----------|----------|----------|----------|----------|----------|--|
|          | 0 [0,0]           | 1 [1,0] | 2 [1,0]*                     | 3 [2,0] | 4 [2,0]* | 5 [2,1] | 6 [2,1]* | 7 [2,2] | 8 [3,0] | 9 [3,0]* | 10 [3,1] | 11 [3,2] | 12 [4,0] | 13 [4,1] | 14 [4,2] | 15 [5,0] |  |
| 0 [0,0]  | 0.052             | 0.044   | ×                            | 0.029   | ×        | 0.005   | ×        | ×       | 0.0024  | ×        | ×        | ×        | ×        | ×        | ×        | ×        |  |
| 1 [1,0]  | 0.428             | 0.038   | 0.317                        | 0.026   | 0.258    | 0.033   | 0.183    | 0.0027  | 0.01    | 0.184    | 0.0012   | ×        | 0.00086  | ×        | ×        | ×        |  |
| 2 [2,0]  | 0.736             | 0.360   | 0.625                        | 0.268   | 0.433    | 0.261   | 0.383    | 0.167   | 0.22    | 0.396    | 0.164    | ×        | 0.144    | ×        | ×        | ×        |  |
| 3 [2,1]  | 0.750             | 0.397   | 0.565                        | 0.308   | 0.206    | 0.293   | 0.167    | 0.197   | 0.258   | 0.179    | 0.185    | 0.651    | 0.176    | 0.503    | 0.439    | 0.430    |  |
| 4 [2,2]  | ×                 | 0.403   | ×                            | 0.198   | ×        | 0.189   | ×        | 0.373   | 0.413   | ×        | 0.328    | ×        | 0.292    | ×        | ×        | ×        |  |
| 5 [3,0]  | 1.010             | 0.663   | 0.828                        | 0.546   | 0.483    | 0.539   | 0.413    | 0.390   | 0.473   | 0.400    | 0.369    | ×        | 0.357    | ×        | ×        | ×        |  |
| 6 [3,1]  | ×                 | 0.697   | ×                            | 0.502   | ×        | 0.479   | ×        | 0.360   | 0.386   | ×        | 0.188    | 0.905    | 0.184    | 0.804    | 0.683    | 0.615    |  |
| 7 [3,2]  | ×                 | ×       | ×                            | ×       | ×        | 0.899   | ×        | ×       | ×       | ×        | 0.748    | 1.01     | ×        | 0.841    | 0.687    | 0.726    |  |
| 8 [4,0]  | ×                 | 0.947   | ×                            | 0.748   | ×        | 0.957   | ×        | 0.851   | 0.627   | ×        | 0.448    | ×        | 0.423    | ×        | ×        | ×        |  |
| 9 [4,1]  | ×                 | ×       | ×                            | ×       | ×        | 1.010   | ×        | ×       | ×       | ×        | 0.895    | 1.107    | 0.763    | 0.855    | 0.813    | 0.763    |  |
| 10 [4,2] | ×                 | ×       | ×                            | ×       | ×        | 1.020   | ×        | ×       | ×       | ×        | 0.815    | 0.964    | ×        | 0.807    | 0.733    | 0.729    |  |
| 11 [5,0] | ×                 | ×       | ×                            | ×       | ×        | 1.144   | ×        | ×       | ×       | 1.010    | 1.152    | 1.008    | ×        | 0.904    | 0.908    | 0.908    |  |

Concerted island diffusion

| Atoms in the island |  | Type | Energy (eV) | Name     | Concerted two-atom diffusion |             |
|---------------------|--|------|-------------|----------|------------------------------|-------------|
|                     |  |      |             |          | Multi-atom type              | Energy (eV) |
| 2                   |  | I2   | 0.062       | Dimer    |                              |             |
| 3                   |  | I3   | 0.161       | Trimer   |                              |             |
| 4                   |  | I4   | 0.182       | Tetramer | C1                           | 0.481       |
| 5                   |  | I5   | 0.222       | Pentamer | C2                           | 0.437       |
| 6                   |  | I6   | 0.201       | Hexamer  | C3                           | 0.397       |
| 7                   |  | I7   | 0.403       | Heptamer | C4                           | 0.228       |
| 8                   |  | I8   | 0.372       | Octamer  |                              |             |

Table A2: Microscopic diffusion activation energy barriers (in eV) for Ni/Cu system.

| Type     | [class, subclass] |         | Single atom diffusion events |         |          |         |          |         |         |          |          |          |          |          |          |          |  |
|----------|-------------------|---------|------------------------------|---------|----------|---------|----------|---------|---------|----------|----------|----------|----------|----------|----------|----------|--|
|          | 0 [0,0]           | 1 [1,0] | 2 [1,0]*                     | 3 [2,0] | 4 [2,0]* | 5 [2,1] | 6 [2,1]* | 7 [2,2] | 8 [3,0] | 9 [3,0]* | 10 [3,1] | 11 [3,2] | 12 [4,0] | 13 [4,1] | 14 [4,2] | 15 [5,0] |  |
| 0 [0,0]  | 0.031             | 0.028   | ×                            | 0.015   | ×        | 0.009   | ×        | ×       | 0.008   | ×        | ×        | ×        | ×        | ×        | ×        | ×        |  |
| 1 [1,0]  | 0.568             | 0.016   | 0.505                        | 0.014   | 0.159    | 0.006   | 0.172    | 0.000   | 0.001   | 0.180    | 0.000    | ×        | 0.023    | ×        | ×        | ×        |  |
| 2 [2,0]  | 0.938             | 0.439   | 0.746                        | 0.364   | 0.743    | 0.389   | 0.541    | 0.305   | 0.500   | 0.562    | 0.319    | ×        | 0.263    | ×        | ×        | ×        |  |
| 3 [2,1]  | 0.800             | 0.489   | 0.550                        | 0.450   | 0.467    | 0.448   | 0.356    | 0.366   | 0.404   | 0.372    | 0.382    | 0.659    | 0.353    | 0.531    | 0.423    | 0.643    |  |
| 4 [2,2]  | ×                 | 0.678   | ×                            | 0.340   | ×        | 0.334   | ×        | 0.596   | 0.283   | ×        | 0.115    | ×        | 0.170    | ×        | ×        | ×        |  |
| 5 [3,0]  | 1.290             | 0.804   | ∞                            | 0.704   | 0.500    | 0.742   | 0.662    | 0.629   | 0.644   | 0.658    | 0.645    | ×        | 0.571    | ×        | ×        | ×        |  |
| 6 [3,1]  | ×                 | 0.875   | ×                            | 0.690   | ×        | 0.693   | ×        | 0.482   | 0.57    | ×        | 0.518    | 0.902    | 0.429    | 0.892    | 0.931    | 0.945    |  |
| 7 [3,2]  | ×                 | ×       | ×                            | ×       | ×        | 1.162   | ×        | ×       | ×       | ×        | 1.144    | 1.191    | ×        | 1.129    | 1.259    | 0.992    |  |
| 8 [4,0]  | ×                 | 1.145   | ×                            | 0.959   | ×        | 1.220   | ×        | 1.157   | 0.858   | ×        | 0.839    | ×        | 0.726    | ×        | ×        | ×        |  |
| 9 [4,1]  | ×                 | ×       | ×                            | ×       | ×        | 1.330   | ×        | ×       | ×       | ×        | 1.384    | 1.209    | 1.225    | 1.400    | 1.226    | 1.000    |  |
| 10 [4,2] | ×                 | ×       | ×                            | ×       | ×        | 1.310   | ×        | ×       | ×       | ×        | 1.120    | 1.291    | ×        | 1.090    | 1.175    | 1.100    |  |
| 11 [5,0] | ×                 | ×       | ×                            | ×       | ×        | 1.507   | ×        | ×       | ×       | 1.382    | 1.482    | 1.326    | ×        | 1.326    | 1.361    | 1.174    |  |

Concerted island diffusion

| Atoms in the island |  | Type | Energy (eV) | Name     | Concerted two-atom diffusion |             |
|---------------------|--|------|-------------|----------|------------------------------|-------------|
|                     |  |      |             |          | Multi-atom                   | Energy (eV) |
| 2                   |  | I2   | 0.021       | Dimer    |                              |             |
| 3                   |  | I3   | 0.148       | Trimer   |                              |             |
| 4                   |  | I4   | 0.157       | Tetramer | C1                           | 0.654       |
| 5                   |  | I5   | 0.220       | Pentamer | C2                           | 0.633       |
| 6                   |  | I6   | 0.199       | Hexamer  | C3                           | 0.294       |
| 7                   |  | I7   | 0.369       | Heptamer | C4                           | 0.218       |
| 8                   |  | I8   | 0.380       | Octamer  |                              |             |

## B1. Results appendix

### B1.1. Additional plots for the total rate and its apparent activation energy

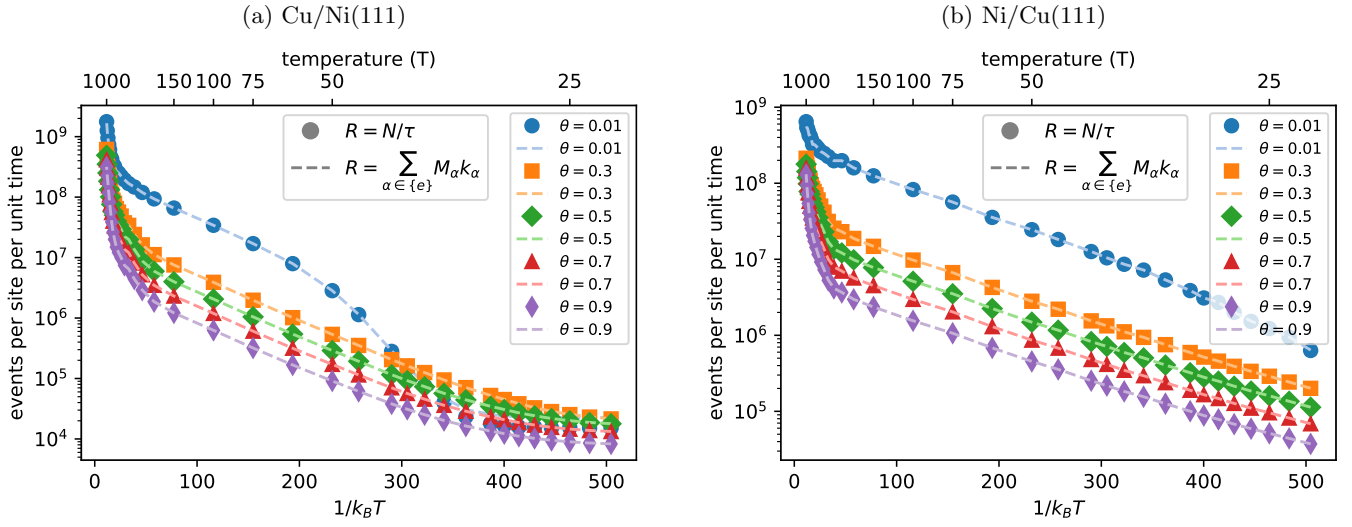


Figure B1: Average total rate per site,  $R = R_d + R_a$ , as a function of inverse temperature for various coverages, as indicated, for (a) Cu/Ni(111), and (b) Ni/Cu(111).

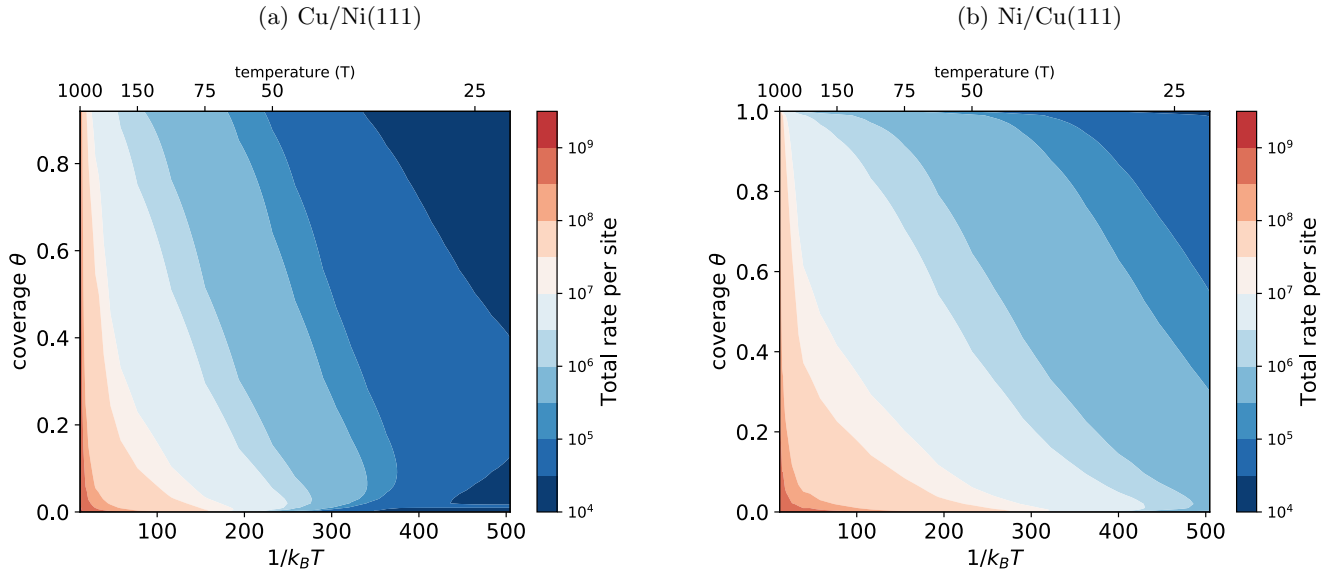


Figure B2: Top view of a three-dimensional plot of the average total rate per site,  $R = R_d + R_a$ , as a function of both coverage and temperature/inverse temperature for (a) Cu/Ni(111), and (b) Ni/Cu(111).

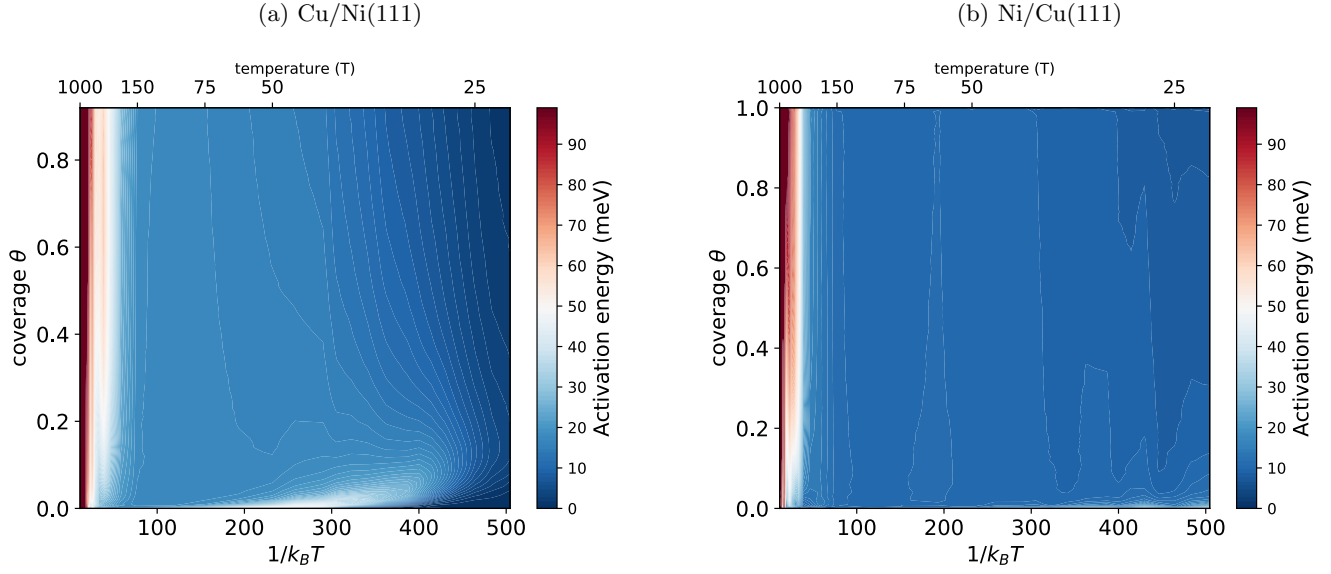


Figure B3: Top view of a three-dimensional plot of the apparent activation energy of the average total rate per site,  $E_{app}^R$ , as a function of both coverage and temperature/inverse temperature for (a) Cu/Ni(111), and (b) Ni/Cu(111).

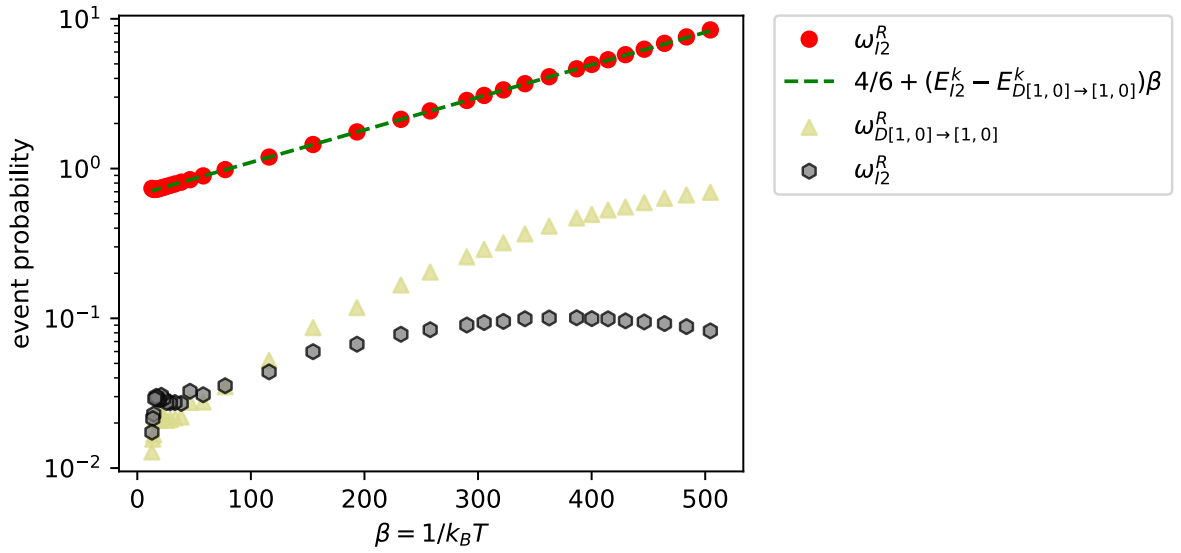


Figure B4: Ratio of the probability to observe non-concerted dimer diffusion to that for concerted diffusion,  $\frac{\omega_{D[1,0] \rightarrow [1,0]}^R}{\omega_{I2}^R} = \frac{M_{D[1,0] \rightarrow [1,0]} k_{D[1,0] \rightarrow [1,0]}}{M_{I2} k_{I2}}$  and the expected result  $\frac{4e^{-E_{D[1,0] \rightarrow [1,0]}^k \beta}}{6e^{-E_{I2}^k \beta}}$ , for Ni/Cu(111) at  $\theta = 0.10$ . This plot confirms that the events  $D[1,0] \rightarrow [1,0]$  and  $I2$  correspond to non-concerted dimer diffusion and concerted dimer diffusion, respectively. Note that the ratio is larger than 1 at low temperatures, indicating that non-concerted dimer diffusion is more probable, while the ratio becomes smaller than 1 at high temperatures, demonstrating that concerted dimer diffusion occurs more frequently.



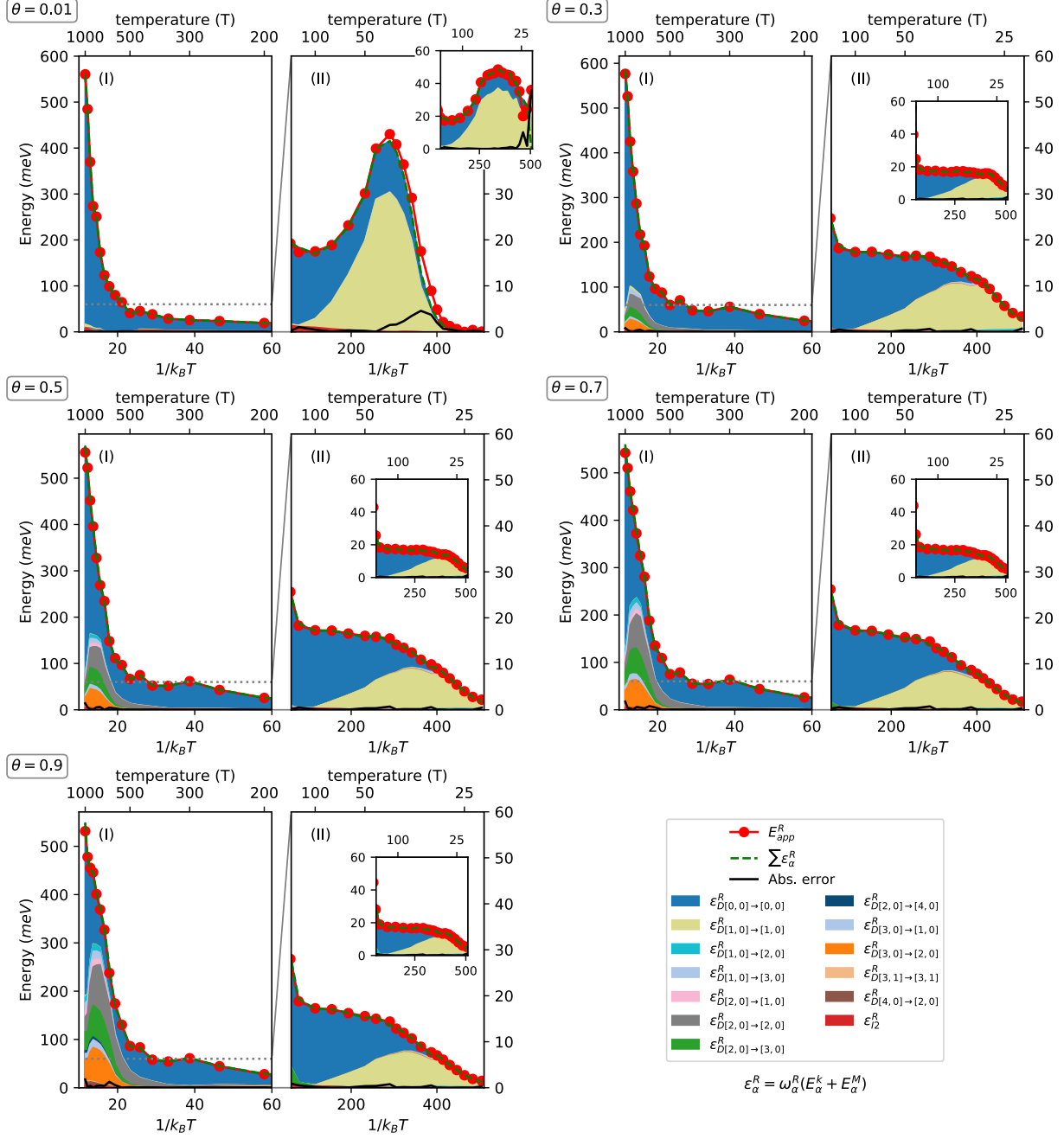


Figure B5: Temperature dependence of  $E_{app}^R$  for Cu/Ni(111) at representative coverage values, as indicated. Two temperature regions are shown: (I)  $1000 \geq T > 150$  K, and (II)  $150 \geq T \geq 23$  K, with region II magnified.  $E_{app}^R$  is described well by  $\sum_{\alpha \in \{e\}} \epsilon_{\alpha}^R$ , where  $\epsilon_{\alpha}^R = \omega_{\alpha}^R (E_{\alpha}^k + E_{\alpha}^M)$ . The absolute error  $|E_{app}^R - \sum_{\alpha \in \{e\}} \epsilon_{\alpha}^R|$  is also plotted. The number of significant contributions to  $E_{app}^R$  increases with coverage and temperature. The insert in region II displays  $E_{app}^R$ .

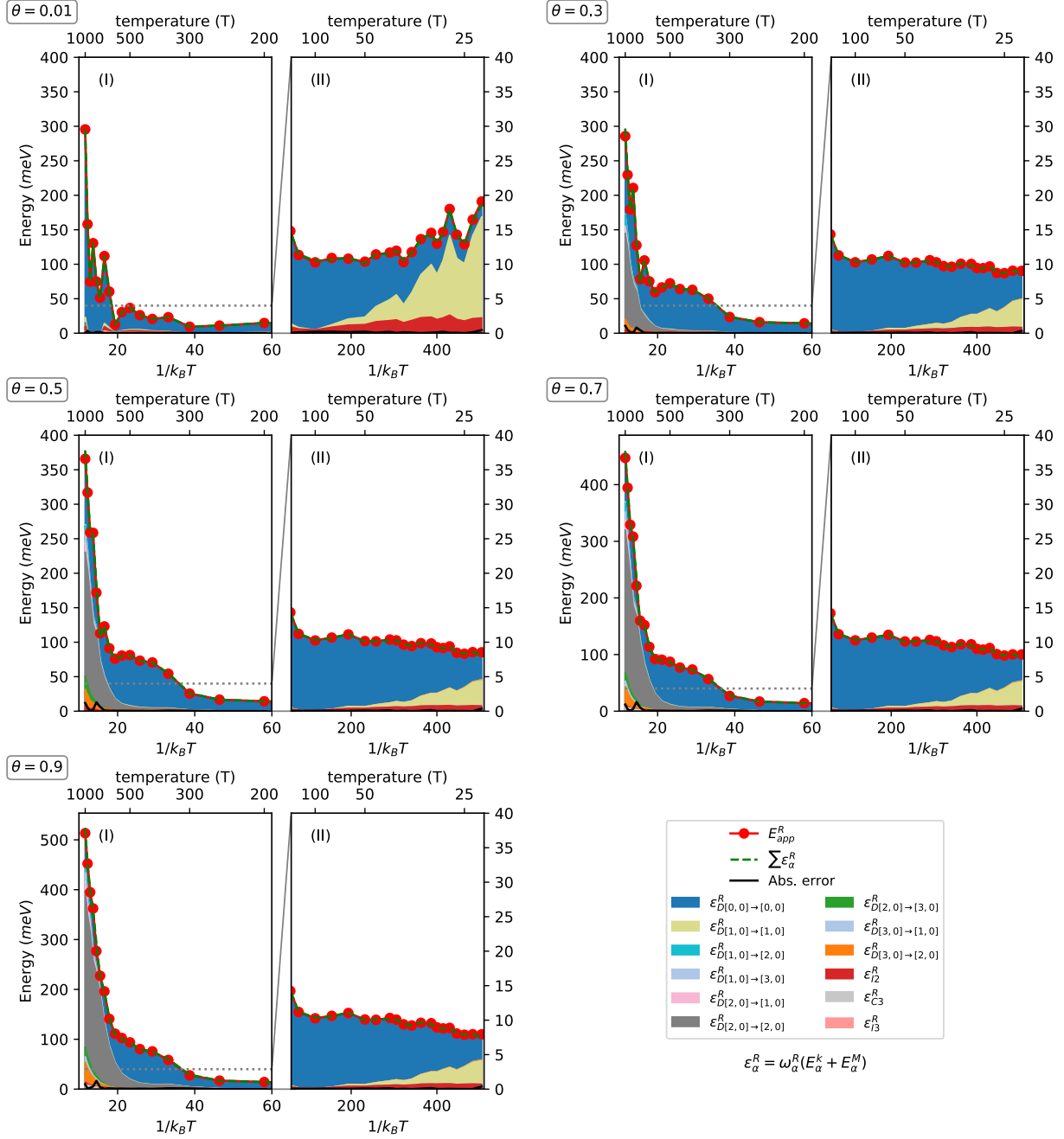


Figure B6: Temperature dependence of  $E_{app}^R$  for Ni/Cu(111) at representative coverage values, as indicated. Two temperature regions are shown: (I)  $1000 \geq T > 150$  K, and (II)  $150 \geq T \geq 23$  K, with region II magnified.  $E_{app}^R$  is described well by  $\sum_{\alpha \in \{e\}} \epsilon_{\alpha}^R$ , where  $\epsilon_{\alpha}^R = \omega_{\alpha}^R (E_{\alpha}^k + E_{\alpha}^M)$ . The absolute error  $|E_{app}^R - \sum_{\alpha \in \{e\}} \epsilon_{\alpha}^R|$  is also plotted. The number of significant contributions to  $E_{app}^R$  increases with coverage and temperature.





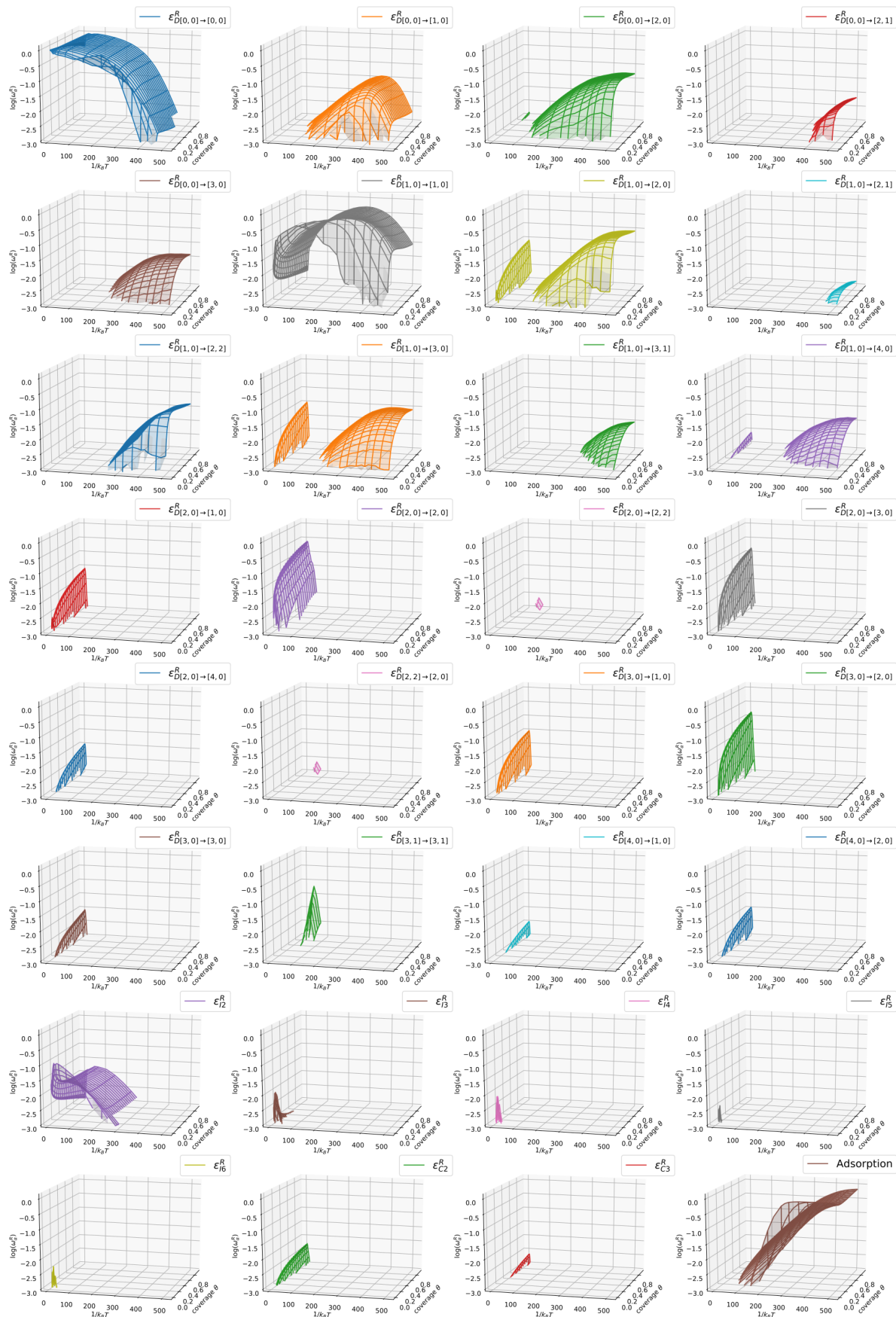


Figure B9: Event probabilities ( $\omega_{\alpha}^R$ ) as a function of coverage and inverse temperature for the most relevant events in the Cu/Ni(111) system.



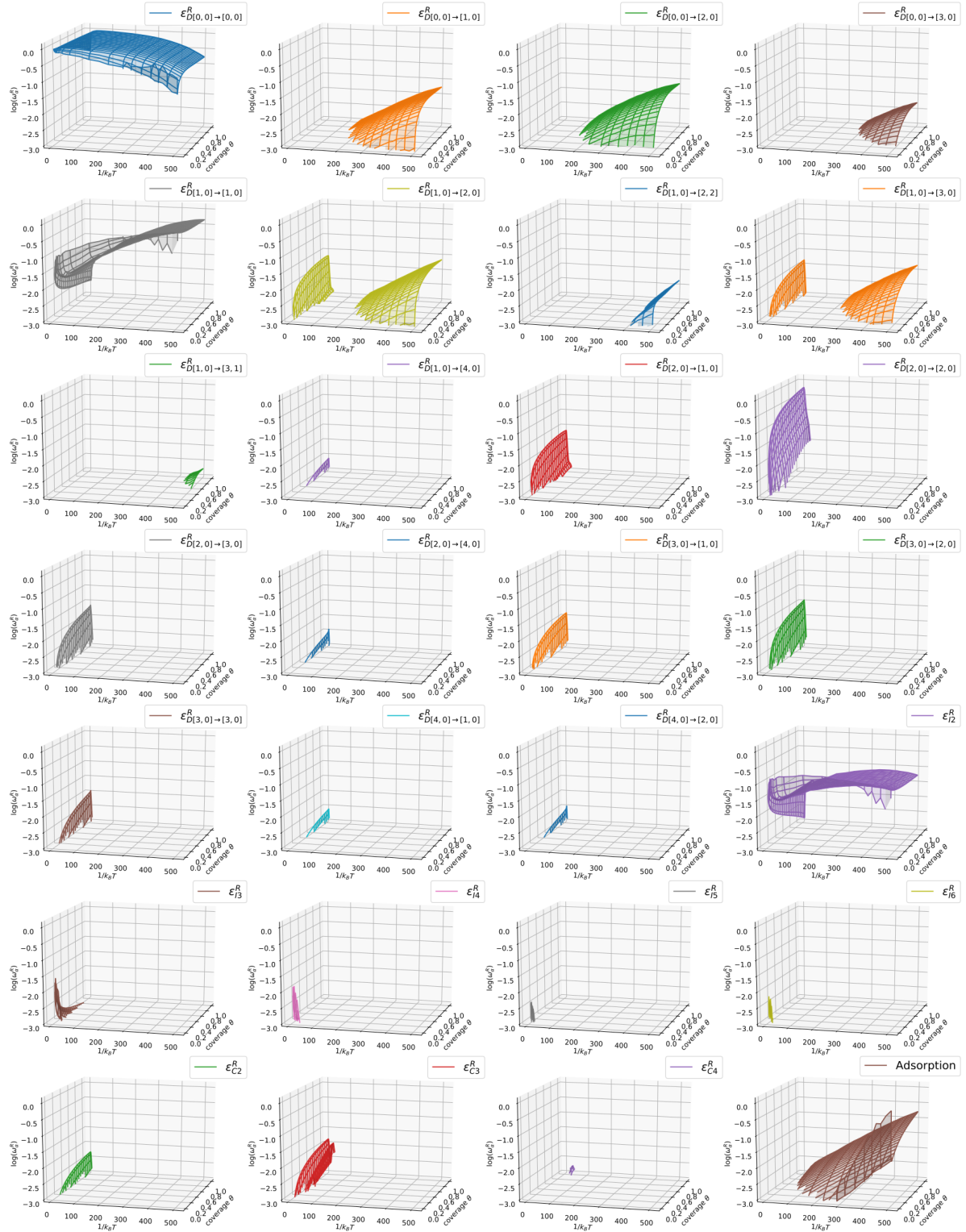


Figure B10: Event probabilities ( $\omega_\alpha^R$ ) as a function of coverage and inverse temperature for the most relevant events in the Ni/Cu(111) system.

### B1.2. Input parameters

Here we show the input parameters required to perform a typical simulation of the present study. The used Git revision of “Morphokinetics” is 2b2811ae1187e69b3c55bf92ccb2c67c87761251. The command to compile the code is “ant jar” and the command to run a simulation is “java -jar dist/morphokinetics.jar”. The latter must be executed within a folder containing the file `parameters`, with the following content (removed the text inside [ ]):

```
{
  "automaticCollections": true,
  "calculationMode": "concerted",
  "cartSizeX": 283,
  "cartSizeY": 283,
  "coverage": 100,
  "depositionFlux": 15000.0,
  "doIslandDiffusion": true,
  "doMultiAtomDiffusion": true,
  "forceNucleation": false,
  "justCentralFlake": false,
  "numberOfSimulations": 10,
  "outputData": true,
  "outputDataFormat": [
    {
      "type": "extra"
    },
    {
      "type": "ae"
    },
    {
      "type": "mko"
    }
  ],
  "psd": false,
  "randomSeed": false,
  "ratesLibrary": "CuNi", [or "NiCu"]
  "temperature": 23, [ranges from 23 to 1000]
  "withGui": false
}
```